The Dynamic Ligand Field of a Molecular Qubit: Decoherence Through Spin–Phonon Coupling

Ruben Mirzoyan and Ryan G. Hadt*

Division of Chemistry and Chemical Engineering, Arthur Amos Noyes Laboratory of Chemical Physics, California Institute of Technology, Pasadena, California 91125, United States

Corresponding Author: rghadt@caltech.edu

Abstract

Quantum coherence of S = ½ transition metal-based quantum bits (qubits) is strongly influenced by the magnitude of spin–phonon coupling. While this coupling is recognized as deriving from dynamic distortions about the first coordination sphere of the metal, a general model for understanding and quantifying ligand field contributions has not been established. Here we derive a general ligand field theory model to describe and quantify the nature of spin–phonon coupling terms in S = ½ transition metal complexes. We show that the coupling term for a given vibrational mode is governed by: 1) the magnitude of the metal-based spin–orbit coupling constant, 2) the magnitude and gradient in the ligand field excited state energy, and 3) dynamic relativistic nephelauxetic contributions reflecting the magnitude and gradient in the covalency of the ligand–metal bonds. From an extensive series of density functional theory (DFT) and time-dependent DFT (TDDFT) calculations calibrated to a range of experimental data, spin–phonon coupling terms describing minimalistic D_{4h}/D_{2d} $[CuCl_4]^{2-}$ and C_{4v} $[VOCl_4]^{2-}$ complexes translate to and correlate with experimental quantum coherence properties observed for Cu(II)- and V(IV)-based molecular qubits with different ligand sets, geometries, and coordination numbers. While providing a fundamental framework and means to benchmark current qubits, the model and methodology described herein can be used to screen any S = ½ molecular qubit candidate and guide the discovery of room temperature coherent materials for quantum information processing.

1. Introduction.

The coupling of electron spin to phonons/vibrations plays important roles in the dynamical properties of transition metal complexes and materials. For example, spin–phonon coupling plays a major role in the photophysical and photochemical properties of transition metal complexes, including ultrafast spin state switching and intersystem crossing, wherein it provides a strong influence on nonequilibrium dynamics.[1–5] It is also a major factor in the magnetization dynamics of single molecule magnets[6–9] and coherent materials for quantum information science.[10–16] Beyond molecular systems, spin–phonon coupling also plays important roles in extended solids and condensed matter (e.g., transition metal oxides) by giving rise to emergent phenomena such as colossal magnetoresistance and high T_C superconductivity,[17–22] including vibrational or optical control of these properties.[23–26] Thus, fundamental studies of spin–phonon coupling can provide insights into a variety of research areas, and there are fascinating intersections between the nature of spin-phonon coupling in molecular systems (e.g., mononuclear, binuclear, and multinuclear transition metal complexes) and extended solids to be explored.

Recent research has focused on the use of S = ½ transition metal complexes as quantum bits (qubits), as the magnetic field split electron spin sublevels ($M_s = \pm 1/2$) provide a two-level system in which a coherent superposition state can be formed. This coherent superposition state, often initiated with a well-defined microwave pulse sequence in an electron paramagnetic resonance (EPR) spectrometer (~9 or 35 GHz for X- or Q-band, respectively), can be leveraged to satisfy DiVincenzo's criteria for the physical implementation of a quantum computer.[27] However, the lifetime of this state must be significantly longer than the gate operation time, and a significant challenge in the domain of molecular qubits is to understand the principles controlling coherence lifetimes. This understanding can then be leveraged for the synthetic design of new transition metal complexes with long-lived coherent states.

The quantities of measure to gauge different complexes are the spin–lattice relaxation time, T_1, the spin-spin lattice relaxation time, T_2, and the phase memory time, T_m, which serves as an "effective" T_2 often measured instead. Recent work has demonstrated the remarkable increase in T_2 when minimizing the quantity of nuclear spins in the environment of the complex, inclusive of both solvent and the ligand set.[28] In these nuclear spin-free environments, T_1 has proved to be the upper bound to coherence lifetimes, which further motivates efforts to better understand contributions to T_1, including the role of the geometric and electronic structure of the transition

metal complex.[28–44] Recent works in this area by Sessoli et al.[13,44], Coronado et al.[14,15], and Freedman et al.[33] have highlighted specific ligand field contributions to spin–phonon coupling and coherence dynamics. Additionally, T_1 relaxation times will also play a major role when molecular qubits are entangled in dimers,[45–49] higher order complexes, or spin-dense arrays,[36] which will be required for the realization of quantum computing applications.

While progress has been made experimentally in elongating T_1 and T_m relaxation times of transition metal complexes at low temperatures (<80 K), very few metal complexes exhibit coherence properties up to room temperature. For example, vanadyl phthalocyanine (VOPc) diluted in a diamagnetic titanyl matrix exhibits room temperature coherence with a T_m of ~1 μs at 300 K, even in the presence of a nuclear spin containing environment.[37] Spin echoes have also been observed up to room temperature in the benzene-1,2-dithiolate (bdt) ligated $(Ph_4P)_2[Cu(C_6H_4S_2)_2]$[33] ($Cu(bdt)_2$) and the maleonitriledithiolate (mnt) ligated $(Ph_4P)_2[Cu(mnt)_2]$[50] ($Cu(mnt)_2$) complexes diluted in diamagnetic Ni lattices. At lower temperatures (~< 80 K), relaxation is dominated by the direct, Raman, and Orbach mechanisms, while a mechanism involving spin–phonon coupling and the modulation of the energy gap between the $M_s = \pm ½$ sublevels dominates at higher temperatures.[51,52] Thus, in order to achieve room temperature coherent materials, spin–phonon coupling and its contribution to T_1 must be better understood. Doing so will allow for direct manipulation of geometric and electronic structure to overcome this barrier. Furthermore, while achieving room temperature coherence is of great technological interest for quantum information processing, these room temperature coherent materials will also provide exciting opportunities for the fundamental studies of spin–phonon coupling and will complement studies of single molecule magnets and photoactive transition metal complexes.

Many of the highest performing S = ½ qubit candidates feature similar structural motifs: 1) a four coordinate square planar Cu(II), or 2) a four coordinate vanadyl moiety featuring a triple bond between the V(IV) and oxo ligand. Comparisons between 1) and 2) and six coordinate, pseudo O_h V(IV) complexes have also been made to highlight structural and electronic contributions to T_1.[13,33,53] As shown below, multiple contributions need to be accounted for in order to make direct comparisons between S = ½ molecular qubits and thus to understand the origins of their coherence times.

Given coherent superposition states are generated within the $M_S = \pm ½$ sublevels of a metal complex, coherence properties are expected to be influenced by the same contributions governing g-values. Ligand field theory (LFT) has provided expressions for understanding geometric and electronic structure contributions to the g-values of Cu(II) complexes.[54] Here this model is extended more generally to a dynamic regime, which allows for the direct understanding of spin–phonon coupling contributions to the g-values of S = ½ transition metal complexes. Using the ORCA program,[55,56] the LFT expressions are further supported by a range of spectroscopically calibrated density functional theory (DFT) and time-dependent DFT (TDDFT) calculations on the well-studied D_{4h} and D_{2d} $[CuCl_4]^{2-}$ and C_{4v} $[VOCl_4]^{2-}$.[57,58] The correlations between experiment and LFT, DFT, and TDDFT calculations have elucidated the key factors that contribute to the nature of spin–phonon coupling terms in S = ½ transition metal complexes, thus providing a detailed orbital and bonding picture for the first time. The model presented here indicates spin–phonon coupling terms are governed by the magnitude of the metal-based spin–orbit coupling (SOC) constant, excited state mixing of orbital angular momentum into the ground state, and dynamic relativistic nephelauxetic contributions. The latter contribution is directly related to the covalencies of ligand–metal bonds and can modify the metal-based SOC constant from that of the free ion in a dynamic manner. Also, correlations between dynamic ground state orbital angular momentum and excited state coupling terms and their relations to spin–phonon coupling terms are drawn for the first time. Specific group theoretical correlations between high and lower symmetry point groups further provide a means to evaluate spin–phonon coupling terms across transition metal complexes and molecular qubits featuring different ligand sets, geometries, and coordination numbers. The model is in excellent agreement with a wide range of experimental quantum coherence properties of Cu(II)- and V(IV)-based molecular qubits and therefore provides a means to rapidly evaluate spin–phonon coupling terms in any S = ½ transition metal complex, including new qubit candidates.

2. Results.

2.1. Dynamic Ligand Field Theory of Cu(II) g-values.

D_{4h} $[CuCl_4]^{2-}$ has a $^2B_{1g}$ (x^2-y^2) ground state (Figure 1). In the absence of SOC, the $^2B_{1g}$ ground state contains no orbital angular momentum and thus would exhibit a g-value of 2.0023 (e.g., g_e of the free electron) in the presence of a magnetic field. However, SOC provides a means for

excited states to mix into the $^2B_{1g}$ ground state and thus introduce orbital angular momentum. This is shown in Figure 1 for D_{4h} $[CuCl_4]^{2-}$. Including SOC, the $^2B_{1g}$ ground state (Γ_7) can mix with both the $^2B_{2g}$ (Γ_7) and ^2E_g ($\Gamma_6 + \Gamma_7$) excited states (Figure 1). From first order perturbation theory, the ground state reflecting the contributions of excited state SOC is:[54]

$$\left|\,^2B'_{1g}\right\rangle = |x^2-y^2\rangle - \frac{\lambda\langle x^2-y^2|\boldsymbol{L}\cdot\boldsymbol{S}|xy\rangle}{E_{B_{2g}}}|xy\rangle - \frac{\lambda\langle x^2-y^2|\boldsymbol{L}\cdot\boldsymbol{S}|xz,yz\rangle}{E_{E_g}}|xz,yz\rangle$$

(equation 1)

where $\lambda = \pm\zeta/2S$ (–830 cm^{-1} for Cu(II)), $\boldsymbol{L}$ and $\boldsymbol{S}$ are the total orbital and spin angular momentum operators, respectively, and $E_{B_{2g}}$ and E_{E_g} are the energies of the $^2B_{2g}$ and ^2E_g excited states, respectively.[54] For greater or less than half-filled electron configurations, either the negative or positive components of $\pm\zeta$ are used, respectively.

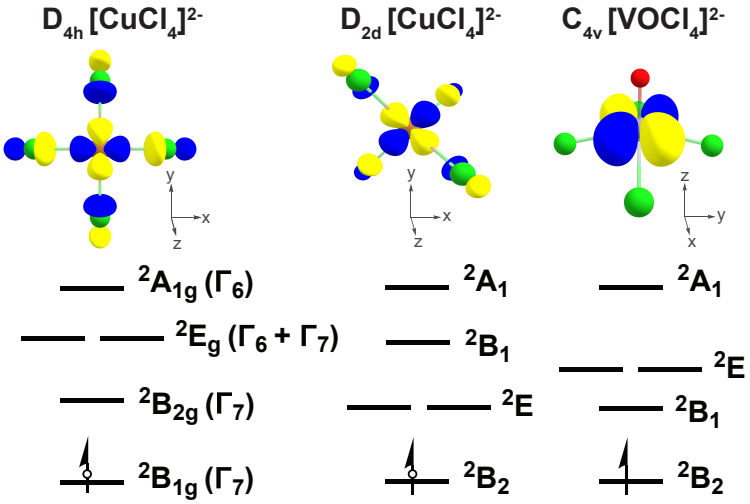

Figure 1. β-LUMOs and qualitative excited state energy diagrams for transition metal complexes considered in the Results sections. The hole formalism is used for $[CuCl_4]^{2-}$, with SOC symmetries given for D_{4h}.

An applied magnetic field will project out different components of $\boldsymbol{L}$ (e.g., $\boldsymbol{L_{x,y,z}}$). Consequently, the magnitude of orbital angular momentum mixing into the ground state is anisotropic. The resulting perturbed ground state wavefunction can be modified to include covalent

ligand–metal interactions. For H || z and taking the covalency of the b_{1g} and b_{2g} orbitals into account, the expression for $g_{||}$ (g_z) becomes:[54]

$$g_{||} = g_e - \frac{8\lambda\alpha_1^2\beta_1^2}{E_{B_{2g}}},$$

(equation 2)

where α_1 and β_1 are the coefficients reflecting the amount of d(xy) and d(x^2-y^2) character, respectively. With H || x,y and considering covalent interactions, equation 2 for $g_\perp$ becomes:

$$g_\perp = g_e - \frac{2\lambda\gamma_1^2\beta_1^2}{E_{E_g}}.$$

(equation 3)

where γ_1 is the coefficient reflecting the d(xz,yz) orbital contribution. From equations 2 and 3, increasing the covalency of the ligand–metal bonds will decrease the deviation from 2.0023 through a relativistic nephelauxetic effect.[59]

The splitting between the ground state $M_s = \pm½$ sublevels and the resulting coherent superposition lifetime is thus sensitive to dynamic behavior of the ligand field excited states and the covalencies of ligand–metal bonds. Fluctuations in the energy gap of a two-level system result in decoherence, and a coherence lifetime has been previously related to the variance in the energy gap by an inverse square root dependence.[60] As the g_z-value and the $M_s = \pm½$ energy gap are directly proportional to one another, the variance in the energy gap can be monitored by proxy of the g-value. Therefore, a descriptor to reflect such fluctuations is the variance in g_z (equation 5). To describe the M vibrational modes denoted by Q_i, we separate the total harmonic vibrational wave function, Ψ_{vib}, as a product of harmonic vibrational wave functions of each mode, Ψ_i, with the vibrational quantum numbers $N = \{n_1, \dots, n_R\}$.

$$\Psi_{vib}^{\mathrm{N}}(Q_1, \dots, Q_R) = \prod_{i=1}^{M} \Psi_{\mathrm{i}}^{n_i}(Q_i)$$

(equation 4)

The variance in g_z can then be expressed as:

$$\mathrm{Var}[g_z] = \langle g_z^2 \rangle - \langle g_z \rangle^2 \approx \frac{\hbar}{2\pi} \sum_{k=1}^{R} \left(\frac{\partial g_z}{\partial Q_i}\right)_e^2 \left(n_i + \frac{1}{2}\right)\left(\frac{1}{v_i m_i}\right) + \frac{\hbar}{4\pi} \sum_{k=1}^{R} \left(\frac{\partial^2 g_z}{\partial Q_i^2}\right)_e^2 \left(n_i^2 + n_i + \frac{1}{4}\right)\left(\frac{1}{v_i^2 m_i^2}\right)$$

(equation 5).

In equation 5, $(\frac{\partial g_z}{\partial Q_i})$ and $(\frac{\partial^2 g_z}{\partial Q_i^2})$ are the equilibrium values of $\frac{\partial g_z}{\partial Q_i}$ and $\frac{\partial^2 g_z}{\partial Q_i^2}$ when $Q_i = 0$, respectively, v_i are the harmonic frequencies, and m_i are the reduced masses. To simplify the treatment of g_z, which depends on the position along a vibrational coordinate Q_i, we separate the normal modes into two types under the harmonic approximation: even modes, where $g_z(Q_{even}) = g_z(-Q_{even})$ and odd modes, where $g_z(Q_{odd}) = -g_z(Q_{odd})$. For the former, at the equilibrium geometry, $\frac{\partial g_z}{\partial Q_{even}} = 0$ and $\frac{\partial^2 g_z}{\partial Q_{even}^2} \neq 0$. For the latter, $\frac{\partial g_z}{\partial Q_{odd}} \neq 0$ and $\frac{\partial^2 g_z}{\partial Q_{odd}^2} = 0$.

Under the harmonic approximation, the first term in the expansion (equation 5) is non-zero for odd modes, while the second term is non-zero for even modes. It is clear from this expression that odd modes have a larger impact on the variance of g_z and consequently the coherence lifetime. $\partial g_z/\partial Q_i$ and $\partial^2 g_z/\partial Q_i^2$ at the equilibrium geometries can be directly related to ligand field parameters in equations 2 and 3. Taking the partial derivative of equation 2 with respect to a vibration coordinate Q_i gives:

$$\partial g_z/\partial Q_i = 8\xi \frac{\eta\left(\partial E_{B_{2g}}/\partial Q_i\right) - E_{B_{2g}}\left(\partial \eta/\partial Q_i\right)}{\left(E_{B_{2g}}\right)^2}$$

(equation 6)

where $\eta = \alpha_1^2\beta_1^2$ and provides adjustments due to covalency. We make the assumption that α_1^2 and β_1^2 change linearly with one another at minimal displacements about the equilibrium position and can therefore be represented by a single "covalency" parameter, η. In the regime where $\eta\left(\partial E_{B_{2g}}/\partial Q_i\right) \gg E_{B_{2g}}\left(\partial \eta/\partial Q_i\right)$, $\partial g_z/\partial Q_i$ will have an inverse square dependence on $E_{B_{2g}}$.

Conversely, when $\eta\left(\partial E_{B_{2g}}/\partial Q_i\right) \ll E_{B_{2g}}\left(\partial\eta/\partial Q_i\right)$, $\partial g_z/\partial Q_i$ will have an inverse dependence on $E_{B_{2g}}$ and a linear dependence with covalency, η. In both cases, the role of the transition energy is clear: The higher the energy separation from the ground state, the lower the $\partial g_z/\partial Q_i$ term by at least an inverse dependence. However, as shown below, the complexes considered here are largely in the regime corresponding to an inverse square dependence on $E_{B_{2g}}$.

For even modes under the harmonic approximation and at the equilibrium geometry, $\partial E_{B_{2g}}/\partial Q_i = \partial\eta/\partial Q_i = 0$. To describe the variance in the energy gap for even modes, a second partial derivative of g_z with respect to the vibrational coordinate is needed.

$$\partial^2 g_z/\partial Q_i^2 = 8\xi\frac{(E_{B_{2g}})(-\partial^2\eta/\partial Q_i^2) + \eta\left(\partial^2 E_{B_{2g}}/\partial Q_i^2\right)}{\left(E_{B_{2g}}\right)^2}$$

(equation 7).

The spin–phonon coupling terms $\partial g_z/\partial Q_i$ and $\partial^2 g_z/\partial Q_i^2$ for odd and even modes, respectively, are therefore related to spectroscopic observables and quantities that are easily calculable. It should be noted that the treatment above has been generated with respect to g_z of D_{4h} Cu(II), but can be done analogously for any S = ½ system. At the very least, the equations above can be used as screening tools to estimate relative coherence lifetimes of molecular qubits by estimating parameters such as the relevant d-d transition energies and covalencies of the ligand–metal bonds, which can be obtained from quantum chemical calculations. The spin–phonon coupling terms in equations 6 and 7 have been computed for a large scope of S = ½ transition metal qubits reported in the literature to establish ligand field principles for manipulating coherence lifetimes.

Below, we utilize D_{4h} and D_{2d} $[CuCl_4]^{2-}$ as structural models to quantitatively evaluate this LFT model using DFT and TDDFT calculations and to define the nature of spin–phonon coupling terms in Cu(II) complexes. This analysis is then translated to C_{4v} $[VOCl_4]^{2-}$ and finally to a variety of Cu(II)- and V(IV)-based molecular qubits reported in the literature.

2.2. Spin–Phonon Coupling Terms in $[CuCl_4]^{2-}$.

2.2.1. D_{4h} $[CuCl_4]^{2-}$.

Depending on the counterion, $[CuCl_4]^{2-}$ can exist in a series of distorted T_d geometries along the D_{4h} to D_{2d} coordinate. This distortion coordinate is governed by the Cl–Cu–Cl angle, α. A broad range of spectroscopic methods have defined the electronic structures of D_{4h} and D_{2d} $[CuCl_4]^{2-}$. By correlating calculations to these data, Solomon et al.[57,58] have developed a spectroscopically calibrated DFT-based methodology that accurately reproduces the experimental data and thus the bonding (e.g., covalency). Key to this description is the incorporation of 38% Hartree-Fock (HF) exchange into the DFT exchange correlation functional.[57,58] This methodology has been used for calculations presented in this section. As discussed in the Methods (see Supporting Information), a calibrated amount of HF exchange is determined independently for each case considered in subsequent sections.

The DFT calculated g-values and excited state energies for an idealized D_{4h} $[CuCl_4]^{2-}$ structure are compared to experiment in Tables 1 and 2, respectively. Note for both D_{2d} and D_{4h} $[CuCl_4]^{2-}$, idealized structures give nearly identical results to those resulting from crystal structures[61]; for a more direct comparison to group theory, only results from the idealized structures are presented here (see Methods in Supporting Information and Table S1a/b for bond distances and angles). Experimentally, the D_{4h} g_z- and $g_{x,y}$-values are 2.221 and 2.040, respectively.[62,63] The calculated values for an idealized geometry based on the X-ray crystallographic structure are 2.204 and 2.056, respectively, in agreement with experiment. The HF dependence of the g_z-value for this structure is given in Figure S1.

A vibrational frequency analysis was carried out using the idealized D_{4h} $[CuCl_4]^{2-}$ structure. The energies, symmetry labels, and scaled vector displacements for all nine normal modes of vibration are given in Table S2a. Using these vibrations, full spin–phonon analyses using the calculated g-values were carried out as described in the Methods section. The coupling terms for g_z ($g_{||}$) are first described, followed by analyses of $g_{x,y}$ ($g_{\perp}$). Briefly, the coupling term for a given g-value and vibrational mode is determined by calculating the g-value along positive and negative distortions about a given normal mode, and the magnitude of the coupling term can be qualitatively estimated by the magnitude of the slope (for odd modes) or curvature (for even modes). The spin–phonon coupling term calculations for the g_z-value of idealized D_{4h} $[CuCl_4]^{2-}$ are given in Figure 2A, and their fits are given in Table S3a. Note these fits are reported for the scaled vibrational

displacements and are converted for comparison purposes when possible to $Å^{-1}$ or $°^{-1}$. The largest coupling term is observed for the totally symmetric a_{1g} breathing mode (mode 7, 296 cm^{-1}), which shows a strong linear dependence between the g_z-value and the vibrational coordinate. Note the calculated frequency for the a_{1g} mode is in fairly good agreement with experimental vibrational energy (276 cm^{-1}).[58] For the a_{1g} mode, a linear fit along the vibrational mode, Q_i, provides a slope of -0.241 g_z/Q_i (0.482 g_z/Å). Interestingly, the spin–phonon coupling terms for the totally symmetric stretch exhibit insightful trends when compared to D_{2d} $[CuCl_4]^{2-}$ and C_{4v} $[VOCl_4]^{2-}$, while also correlating with experimental coherence properties as discussed below.

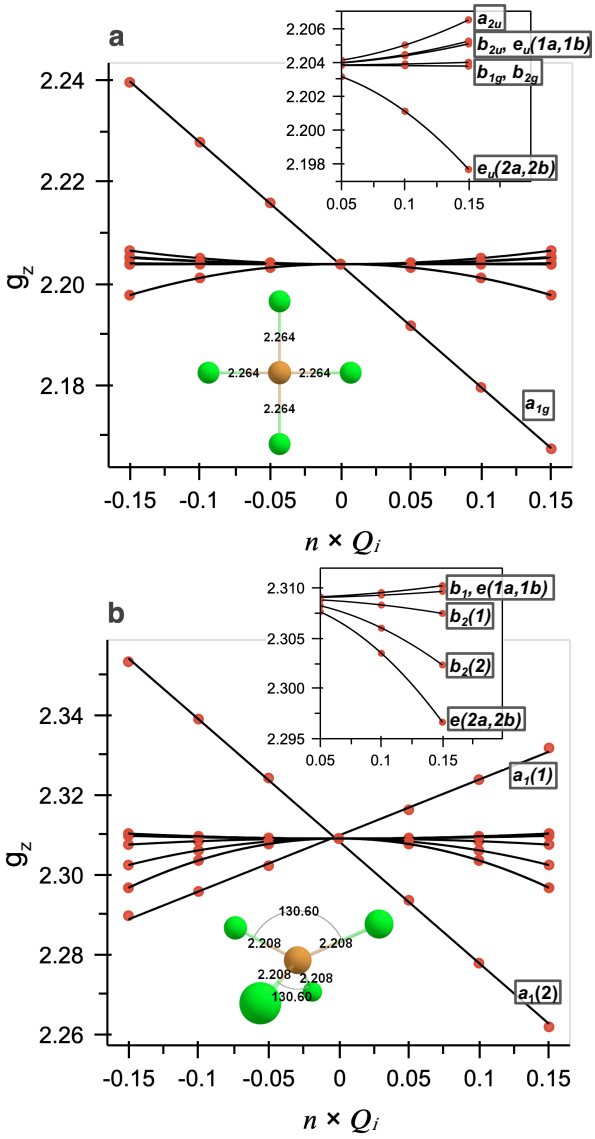

Figure 2. Evolution of the g_z-values along each normal mode of vibration for idealized structures of (a) D_{4h} and (b) D_{2d} $[CuCl_4]^{2-}$. Insets provide zoomed in views for positive distortion and pictorial representations of the respective molecules.

Of the other vibrational modes, 1 (b_{2u}, –86 cm^{-1}), 2 (a_{2u}, 140 cm^{-1}), 3/4 (e_u *(1a, 1b)*, 172 cm^{-1}), and 8/9 (e_u *(2a, 2b)*, 342 cm^{-1}) are even modes with quadratic coupling terms. The a_{2u} and e_u *(2a, 2b)* modes exhibit the largest coupling terms (0.119 and -0.272 g_z/Q_i, respectively) and involve motion of the metal out-of-plane and in-plane, respectively (Table S2a). For the a_{2u} mode, the slope can be better quantified by using the amount of metal displacement and gives 0.216 g_z/Å. The coefficients for the b_{2u} and e_u *(1a, 1b)* modes are -0.063 and -0.056 g_z/Q_i, respectively. While the quadratic spin–phonon coupling terms of the e_u *(2a, 2b)* modes are the largest, they also have the highest calculated frequencies (342 cm^{-1}) and are therefore not considered in detail here, as these modes will not be as thermally populated past their zero-point energies at practical temperatures. Finally, modes 5 (b_{2g}, 183 cm^{-1}) and 6 (b_{1g}, 198 cm^{-1}) exhibit negligible spin–phonon coupling terms with the g_z-value (Table S3a). Note, however, the corresponding coupling terms are substantially smaller when the magnetic field is oriented along $\boldsymbol{L_x}$ or $\boldsymbol{L_y}$ (i.e., for $g_{x,y}$-values). Also, the spin–phonon coupling term for the b_{2u} mode is increased substantially in the D_{2d} structure. These observations are discussed further below.

Table 1. Comparisons between a variety of experimental and calculated g-values for D_{4h} and D_{2d} $[CuCl_4]^{2-}$ and other Cu(II) complexes.

Molecule	g_z		g_y		g_x	
	Exp.	**Calc.**	**Exp.**	**Calc.**	**Exp.**	**Calc.**
D_{4h} $[CuCl_4]^{2-}$ [a]	2.221	2.204	2.040	2.057	2.040	2.054
D_{4h} $[CuCl_4]^{2-}$ [b]	2.221	2.204	2.040	2.056	2.040	2.056
D_{2d} $[CuCl_4]^{2-}$ [a,c]	2.435	2.304	2.079	2.123	2.079	2.065
D_{2d} $[CuCl_4]^{2-}$ [b]	2.435	2.309	2.079	2.095	2.079	2.095
$[Cu(mnt)_2]^{2-}$ [d]	2.091	2.085	-	2.039	-	2.036
CuPc [e]	2.199	2.163	2.052	2.026	2.052	2.026
CuN_4 (H) [f]	2.19	2.196	-	2.055	-	2.063
CuN_4 (Me) [f]	2.205	2.218	-	2.053	-	2.078
CuN_4 (t-Bu) [f]	2.28	2.273	-	2.049	-	2.141
$[Cu(bdt)_2]^{2-}$ [g]	2.085	2.047	2.019	2.015	2.019	2.016
$[Cu(bds)_2]^{2-}$ [h]	2.082	2.089	2.018	2.053	2.018	2.031

[a] Crystal structure from ref. 61, g-values from ref. 62.
[b] Idealized structure from crystal structure.
[c] g-values from ref. 63.
[d] Crystal structure and g-values from ref. 14.
[e] DFT optimized structure, g-values from ref. 72.
[f] DFT optimized structure, experimental g-values from ref. 69.
[g] Crystal structure from ref. 73, g-values from ref. 33.
[h] Crystal structure and g-values from ref. 33.

Table 2. Comparisons between experimental and calculated ligand field transitions for D_{4h} and D_{2d} $[CuCl_4]^{2-}$.

Exp. (cm^{-1})[c]	Assignment	Calc. (cm^{-1})[a]	Calc. (cm^{-1})[b]	Exp. (cm^{-1})[c]	Assignment	Calc. (cm^{-1})[a]	Calc. (cm^{-1})[b]
D_{4h}				D_{2d}			
12000	$^2B_{1g} \rightarrow {}^2B_{2g}$	14470	14475	5500	$^2B_2 \rightarrow {}^2E$	6470	6825
13500	$^2B_{1g} \rightarrow {}^2E_g$	14525	14610			7360	6825
		14685	14610	8000	$^2B_2 \rightarrow {}^2B_1$	10465	10440
16500	$^2B_{1g} \rightarrow {}^2A_{1g}$	15485	15485	9400	$^2B_2 \rightarrow {}^2A_1$	9130	9005

[a] X-ray crystal structure from ref. 61.
[b] Idealized structure from crystal structure.
[c] Experimental d-d transitions from ref. 64.

Given the ligand field origin of the SOC induced mixing of orbital angular momentum into the $^2B_{1g}$ ground state (Figure 1), an analysis of the excited state energies was also carried out. Comparisons between experimental and calculated ligand field transitions are given in Table 2. Experimentally, the $^2B_{2g}$, ^2E_g, and $^2A_{1g}$ ligand field transitions of D_{4h} $[CuCl_4]^{2-}$ are observed at 12000, 13500, and 16500 cm^{-1}, respectively.[64] From equation 2, the $^2B_{2g}$ excited state can introduce ground state orbital angular momentum through SOC, and the g_z-value is inversely dependent on the ligand field energy. A TDDFT calculation gives an energy of 14470 cm^{-1}, in fairly good agreement.

The vibrational analysis of the $^2B_{2g}$ ligand field excited state is given in Figure 3a, and their fits are given in Table S3a. Note the calculation of the ligand field energy along a given vibrational mode provides the excited state coupling term, which takes into account the displacement between the ground and excited state potential energy surfaces (Figure 4a). This displacement of the excited surface relative to the ground state results in a distorting force along a normal mode, Q_i, in the excited state. This distorting force can be estimated by evaluating the effect of electron-nuclear coupling on the total energy of the excited state, E_{ES}:[54]

$$E^e_{elec-nuc} = \left\langle \psi_e^{elec} \middle| \frac{\partial E_{ES}}{\partial Q_i} \middle| \psi_e^{elec} \right\rangle Q_i$$

(equation 8)

For non-zero values of this integral, the excited state will distort along Q_i by a value ΔQ_i; the excited state coupling term is determined by calculating the energy change in the electronic transition to ψ_e with a change along the coordinate Q_i. This is shown qualitatively for D_{4h} and D_{2d} structures in Figure 4a. The partial derivative ($\partial E/\partial Q_i$) reflects the relative curvature of the excited state potential energy surface near the ground state equilibrium geometry (i.e., in the vicinity of the Franck-Condon region). The excited state coupling term therefore provides a means to quantify the change in excited state orbital angular momentum that can SOC into the ground state along a given vibrational coordinate.

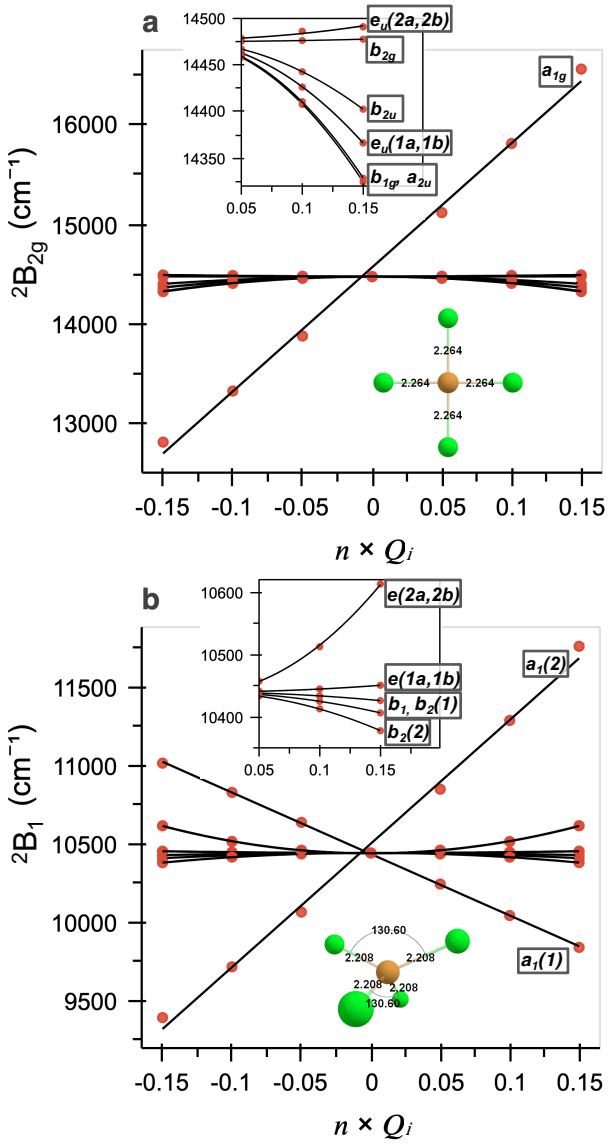

Figure 3. Evolution of the d(x^2-y^2) → d(xy) transition energies for (a) D_{4h} and (b) D_{2d} $[CuCl_4]^{2-}$.

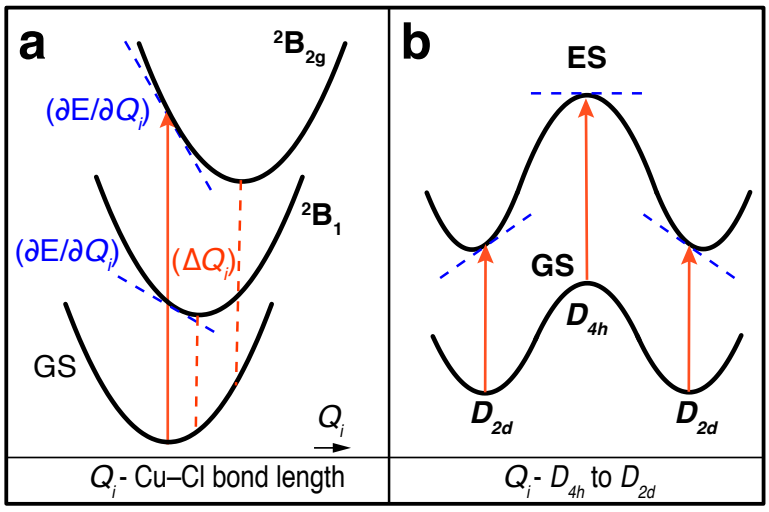

Figure 4. Qualitative potential energy surfaces of $[CuCl_4]^{2-}$. (a) Excited state linear coupling terms for the totally symmetric Cu–Cl stretch, and (b) change in the excited state linear coupling term upon distorting from D_{4h} to D_{2d}. To simplify (a), the ground state potential energy surfaces of D_{4h} and D_{2d} are overlaid even though their Cu–Cl bonds do not have the same equilibrium distance.

As with the g_z-value analysis, the totally symmetric a_{1g} mode exhibits the largest coupling term for the $^2B_{1g}$ excited state (Figure 3a). The slope of the a_{1g} mode is 12405 cm^{-1}/Q_i, which gives -24940 cm^{-1}/Å. That is, the energy of the $^2B_{1g}$ state decreases as the ligand–metal bonds are elongated and vice versa. The quadradic terms for the a_{2u} mode are -6700 cm^{-1}/Q_i and -12230 cm^{-1}/Å. Note the slopes and curvatures of the $^2B_{2g}$ energy are inverted relative to those for the g_z-value slope (Figure 2a). This behavior is consistent with equation 2 and the inverse energy dependence on SOC. The other modes discussed above that exhibit spin–phonon coupling terms with the g_z-value also exhibit inverted behavior. For example, the a_{2u} and b_{2u} modes exhibit positive quadratic behaviors in Figure 2a and negative ones in Figure 3a. Note the b_{1g} mode does not exhibit a substantial coupling term for the g_z-value but does with the $^2B_{2g}$ energy. This is due to the nature of the b_{1g} vibrational distortion (see Table S2a), which lowers the symmetry from D_{4h} to D_{2h} by making two of the Cu(II)–Cl bonds, and thus the x- and y-axes, inequivalent. This turns on a small mixing between a forbidden (in D_{4h}) $^2A_{2g}$ charge transfer state and the $^2B_{2g}$ ligand field state. Both of these states transform as $^2B_{1g}$ upon lowering symmetry to D_{2h}. The energy of the forbidden $^2A_{2g}$ state exhibits a strong dependence on the b_{1g} mode distortion. Thus, we ascribe the energy shift of

the $^2B_{2g}$ state observed in Figure 3a to this mixing. Also, other than e_u *(2a, 2b)* modes, no other modes exhibit this distortion induced mixing, and they maintain their original ligand field compositions observed for the D_{4h} structure. Thus, the excited state coupling term (equation 8) for the $^2B_{1g} \rightarrow {}^2B_{2g}$ excitation provides a means to evaluate the vibrationally induced change in ground state orbital angular momentum and its effect on the g_z-value.

In addition to excited state SOC, equation 2 indicates covalency contributions are important determinants of molecular g-values. Experimentally, the Cu(d) character for D_{4h} $[CuCl_4]^{2-}$ is 0.62 ± 0.2.[57,58] The β-LUMO of the model considered here is given in Figure 1 and reflects a total Cu(d) character and spin density of 65 % and 0.668 from Loewdin population analysis and spin density, respectively. Importantly, as shown below, the measure of covalency at the equilibrium geometry, by proxy of the spin density, is a key determinant to understanding its role in spin–phonon coupling terms. Thus, the 38 % HF method applied to a complex with known Cu(d) character provides an excellent starting point. Fits for the spin-phonon coupling term analyses using Cu spin densities are given in Table S3e. The fits for the a_{1g} mode give values of -0.157 SD/Q_i and 0.221 SD/Å. As observed above for g_z-values and the $^2B_{2g}$ energies, the largest coupling term for Cu spin density is observed for the totally symmetric a_{1g} mode. For this mode, the change in covalency along the a_{1g} coordinate contributes in the same direction/sign to the change in g_z-value as the $^2B_{2g}$ ligand field energy. This is also the case for the b_{2u} mode. The concerted contribution from ligand field energies and covalency is not observed for all modes, however. From example, the Cu spin density contribution for the a_{2u} mode opposes the contribution to the g_z-value from the $^2B_{1g}$ excited state and illustrates an important interplay between excited state SOC and covalency to the resulting spin–phonon coupling term for the g_z-value.

The individual contributions to the g_z-value from the $^2B_{1g}$ energy and Cu spin density can be estimated using equation 2 in combination with the DFT and TDDFT calculations. For example, for D_{4h} $[CuCl_4]^{2-}$, using the calculated Cu spin density of 0.668 and the $^2B_{1g}$ energy of 14475 cm^{-1}, equation 2 predicts a g_z-value of 2.205. This is similar to the DFT calculated g_z-value (2.204). For each mode, the relative change in spin density and/or $^2B_{1g}$ energy can be used to estimate a change in g_z-value. The g_z-value estimated from equation 2 can thus be compared directly to the DFT calculated change in g_z-value along each vibrational coordinate. These plots for all normal modes and each g-value are given in Figures S3-S5; the results for the b_{2u}, a_{2u}, and a_{1g} modes are given in Figures 5 (a-c), respectively. From these comparisons for the b_{2u} mode (Figure 5a), the

Cu spin density and $^2B_{2g}$ energy both contribute appreciably to the change in g_z-value. Furthermore, for the a_{2u} mode (Figure 5b), the change in g_z-value is largely due to the change in the $^2B_{2g}$ energy; as mentioned above, a small component from the Cu spin density component actually opposes the change in g_z-value determined by the $^2B_{2g}$ energy alone. Lastly, for the a_{1g} mode, the change in the g_z-value is largely due to the change in $^2B_{2g}$ energy, but the spin density component contributes to a small extent. Thus, this analysis (Figure 5 and Figures S3-S5) provides a means to qualitatively decompose the spin–phonon coupling term contributions from ground state covalency and orbital angular momentum from excited state SOC.

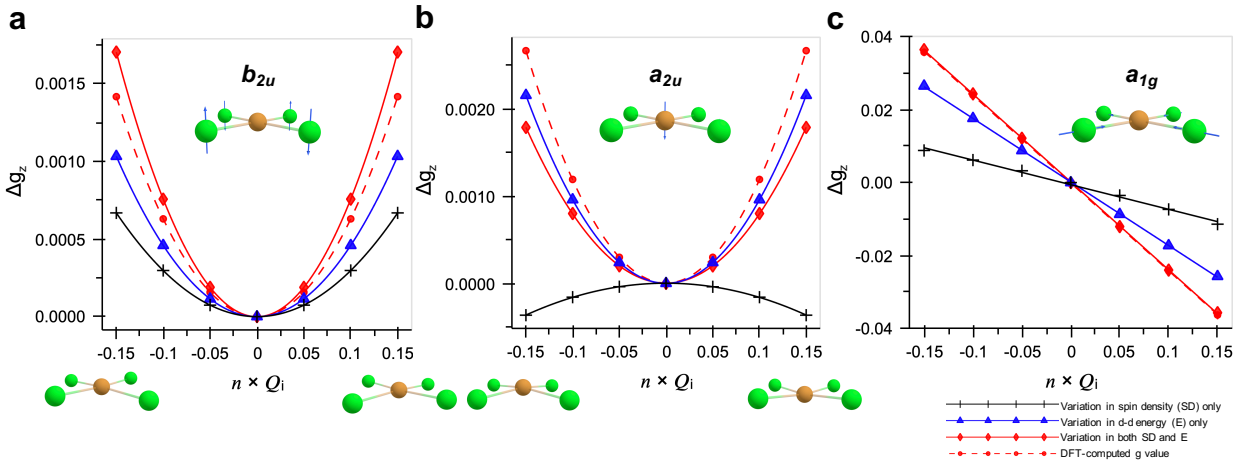

Figure 5. Independent contributions from d-d transition energy and ligand–metal covalency to the change in g_z for D_{4h} $[CuCl_4]^{2-}$. Comparisons are made between the Δg_z as calculated from the LFT expression and as computed using ORCA for modes (a) b_{2u}, (b) a_{2u}, and (c) a_{1g}. For these plots, the square of the spin density on Cu was used as a proxy for the covalency. Vector displacements are provided for each vibrational distortion.

The spin–phonon coupling terms for the $g_{x,y}$-values for the D_{4h} structure are given in Figure S9, with the corresponding fits given in Table S3b and S3c.The coupling terms for the g_x- and g_y-values are very similar except for the inversion of the e_u modes (e.g., the *1a/2a* components switch with the *2a/2b* components). As with the g_z-value, the largest coupling term for the $g_{x,y}$-values is observed for the a_{1g} mode (-0.072 g_z/Q_i,). However, the coupling term for the $g_{x,y}$-values is significantly less than that observed for g_z-values (-0.241 g_z/Q_i) by a factor of ~3.3. This difference reflects the ratio of the prefactors given in equations 2 and 3, as well as contributions from anisotropic covalency. The other modes show a similar behavior between g_x- and g_z-values and therefore are not discussed here. However, while the b_{1g} mode exhibited a negligible spin–phonon

coupling term for the g_z-value (Figure 2a), it exhibits a larger coupling term for the $g_{x,y}$-values (Figures S8a/b). Thus, the main differences between the g_z and $g_{x,y}$ regions is the magnitude and anisotropy of the spin–phonon coupling terms, with different vibrational modes (e.g., b_{1g} mode) being selectively activated in the $g_\perp$ region.

The corresponding spin–phonon coupling terms of the two components of the ^2E_g excited state are given in Figure S10. The correlation between the $g_{x,y}$-values and the excited state SOC is similar to that laid out for the g_z-value and is therefore not addressed further here.

In summary for D_{4h} $[CuCl_4]^{2-}$, up to the totally symmetric stretch, the vibrational modes that exhibit the largest spin–phonon coupling terms are the a_{2u} and a_{1g} modes, with the b_{2u} and e_u *(1a, 1b)* modes having smaller coupling terms. Excited state SOC and covalent contributions are both important quantifiers and determinants of spin–phonon coupling terms, and they can either work cooperatively or oppose one another (Figure 5). Lastly, the spin–phonon coupling terms are anisotropic between the $g_{\parallel}$ and $g_\perp$ regions, with a general decrease in coupling terms in the $g_\perp$ region and an activation of different vibrational modes. This anisotropy may be an interesting way to experimentally probe and explore spin–phonon coupling terms in transition metal complexes and qubits.

2.2.2. D_{2d} and Comparisons to D_{4h} $[CuCl_4]^{2-}$.

Experimentally, going from D_{4h} to D_{2d} $[CuCl_4]^{2-}$, the g-values shift from 2.221 and 2.040 to 2.435 and 2.079, respectively (Table 1). The experimental increase in g-values is reproduced by the DFT calculated g-values (2.309 and 2.095, respectively). In addition, the ligand field strength decreases significantly upon distorting to D_{2d}, which results in a decrease in the ligand field transition energies to 5500, 8000, and 9400 cm^{-1}. The transition at 8000 cm^{-1} is the $^2B_2 \rightarrow {}^2B_1$ transition, which is predicted at 10440 cm^{-1} using TDDFT. Note in going from D_{4h} to D_{2d} group theory requires the ground state transform as $^2B_2$ (Figure 1).[64] While this formally leads to a switch of the ground state from x^2-y^2 to xy, the overall orientation of the orbital with respect to the ligand–metal bonds does not change upon lowering symmetry from D_{4h} to D_{2d}, and we therefore retain the x^2-y^2 labeling as done previously.[54] Translating to the D_{2d} structure decreases the overlap between the Cu d(x^2-y^2) orbital and the ligand p orbitals, which results in a decrease in the covalency of the Cu–Cl bonds and thus a larger Cu spin density. As done above for D_{4h}, using the DFT calculated

spin density, the $^2B_1$ ligand field energy, and equation 2 predicts a g_z-value of 2.361, which is in the range of that predicted from the DFT calculation (2.309).

The spin–phonon analysis for the g_z-value of D_{2d} $[CuCl_4]^{2-}$ is given in Figure 2B (fits given in Table S4a). Note that group theory provides a means to directly correlate the vibrational modes between the D_{4h} and D_{2d} structures. These correlations are applied here and are reflected in the labels of the D_{2d} figures and tables throughout. As observed for the D_{4h} structure, the largest coupling term for the D_{2d} structure is observed for the totally symmetric breathing mode, $a_1(2)$ (mode 7, Table S3) (a_{1g} in D_{4h}). For the $a_1(2)$ mode, a linear fit along the vibrational mode, Q_i, provides a slope of -0.306 g_z/Q_i (0.612 g_z/Å). These slopes are larger than those observed for the a_{1g} mode in the D_{4h} structure (-0.241 g_z/Q_i and 0.482 g_z/Å). Furthermore, while no other modes exhibited substantial linear coupling terms in the D_{4h} structure, from the spin–phonon analyses in Figure 2B, the $a_1(1)$ mode (mode 1 in both D_{4h} and D_{2d}; b_{2u} in D_{4h}) becomes activated and linear in the D_{2d} structure. For the $a_1(1)$ mode, the linear fit along the vibrational mode, Q_i, provides a slope of 0.140 g_z/Q_i. The activation of the $a_1(1)$ mode and the observation of linear coupling term behavior upon going to the D_{2d} structure is discussed below.

The quadratic coefficient of the $b_2(1)$ mode of the D_{2d} structure (-0.068 g_z/Q_i) is reduced relative to the D_{4h} structure (0.119 g_z/Q_i) (a_{2u} in D_{4h}). Of the modes with frequencies less than the $a_1(2)$ totally symmetric stretch, the $b_2(2)$ mode has a quadratic coefficient of -0.295 g_z/Q_i, which is activated relative to the D_{4h} structure in which a very small coupling term was observed (b_{1g} in D_{4h}).

The spin–phonon analysis for the $^2B_1$ excited state of D_{2d} $[CuCl_4]^{2-}$ is given in Figure 3B. Both $a_1(2)$ and $a_1(1)$ modes exhibit oppositely signed slopes between Figure 2B and 3B, indicating appreciable contributions to the spin–phonon coupling term from excited state SOC. For the $a_1(2)$ mode, the linear fit along the vibrational mode, Q_i, provides a slope of 7885 cm^{-1}/Q_i (-15770 cm^{-1}/Å). Interestingly, these slopes are smaller than those observed for the a_{1g} mode in the D_{4h} structure (12405 cm^{-1}/Q_i and -24940 cm^{-1}/Å). The larger slope for the D_{4h} structure might suggest it would have a larger spin–phonon coupling term. However, equation 2 and its differentiated forms predict important behavior in this regard when comparing the D_{4h} and D_{2d} structures. This behavior is addressed below.

The slope of the $a_1(1)$ mode for the D_{2d} structure is -3925 cm^{-1}/Q_i, which is roughly half that observed for the $a_1(2)$ mode (7885 cm^{-1}/Q_i). The activation of this mode is a direct

consequence of the symmetry about the Cu complex and its effect on the excited state coupling term (equation 8). This is shown pictorially in Figure 4b. For the D_{4h} structure, the b_{2u} mode is imaginary, representing a saddle point on the ground state potential energy surface. It has also been stressed that the D_{4h} $[CuCl_4]^{2-}$ structure arises due to crystal packing forces, and the D_{2d} structure represents the energetic minimum on the ground state potential energy surface.[57] However, the symmetry of the complex has important consequence for the excited state coupling term and thus the spin–phonon coupling terms. In the D_{4h} structure, the excited state that can SOC with the ground state is at an energetic maximum along the b_{2u} (in D_{4h}) mode connecting the D_{4h} and D_{2d} structure. Upon distorting along this mode, both the ground and excited state energies are reduced. At the ground state minimum the excited state potential energy surface is shifted relative to the ground state surface. This offset gives rise to a non-zero excited state coupling term for the D_{2d} structure. As discussed above, a non-zero excited state coupling term provides a mechanism for the amount of orbital angular momentum mixed into the D_{2d} ground state to change along the vibrational mode. This mixing is prohibited in the D_{4h} ground state. In some ways, this qualitatively resembles atomic clock transitions that have also been utilized in the development of qubits.[35,65–68]

The spin density as a function of the vibrational coordinate for the D_{2d} structure is given in Figure S2B. The slopes for the $a_1(2)$ mode are -0.157 SD/Q_i and 0.315 SD/Å. These are larger than the values for the a_{1g} mode in the D_{4h} structure (-0.111 SD/Q_i and 0.221 SD/Å). As done for the D_{4h} structure, the individual contributions to the g_z-value from the $^2B_{1g}$ energy and Cu spin density can be estimated using equation 2. These results are given in Figures S6-S8.

The spin–phonon analyses were extended to the $g_{x,y}$-values of D_{2d} $[CuCl_4]^{2-}$. These results are given in Figure S11 and Tables S4b and S4c. The corresponding vibrational analyses are for the ^2E excited state of D_{2d} $[CuCl_4]^{2-}$ are given in Figure S12 and Tables S4b and S4b. Similar to D_{4h}, there are new modes that are activated for the $g_{x,y}$-values. For the D_{2d} structure, these include the $b_2(1)$ and $b_2(2)$ modes.

In summary, for D_{2d}, in addition to the $a_1(2)$ mode, a linear spin–phonon coupling term in the $a_1(1)$ mode (i.e., the b_{2u} parent mode in D_{4h}) becomes activated. This is anticipated to be especially important for local mode contributions to decoherence, as the $a_1(1)$ mode is the lowest energy mode in these structures and thus can become populated at relatively low temperatures. Indeed, all Cu(II)-based qubits in the literature are roughly square planar, D_{4h}. Insightful and

quantitative comparisons can be drawn between the vibrational analyses of the total symmetric breathing modes of the D_{4h} and D_{2d} structures, with the latter exhibiting a larger spin–phonon coupling term. This larger coupling term occurs even though the excited state coupling term (Figure 4a) is larger than the D_{2d} structure. The activation of the $a_1(1)$ mode for the D_{2d} structure and its excited state coupling behavior can be understood via the qualitative potential energy surfaces in Figure 4b. Given the ground state structure of $[CuCl_4]^{2-}$ in the absence of any structural constraints is D_{2d}, going to the D_{4h} structure on the ground state surfaces results in a scenario where there is a relatively small gradient in the excited state potential energy surfaces. Thus, for the D_{4h} structure, there is little change in the ground state orbital angular momentum upon fluctuations in the b_{2u} mode that provides a coordinate between the D_{4h} and D_{2d} structures. However, the excited state potential energy surface is offset from the ground state surface near the equilibrium position of the D_{2d} geometry, which allows for larger changes in ground state orbital angular momentum for the $a_1(1)$ mode.

2.2.3. Cu(II) Effective Decoherence Maps and Comparisons to Ligand Field Theory.

For D_{2d} $[CuCl_4]^{2-}$, the vibrational modes with by far the largest spin–phonon coupling terms were those of $a_1(1)$ and $a_1(2)$ symmetry, and are consequently expected to be the most impactful to the quantum decoherence of Cu(II) complexes. The $a_1(1)$ mode can be described by the Cl–Cu–Cl bond angle, α, while the $a_1(2)$ mode can be described by the Cu–Cl bond distance. Effective decoherence maps have been generated spanning this space of $[CuCl_4]^{2-}$ geometries (Figure 6 (a-c)). In Figure 6, the magnitude and direction of g_z-value gradients (i.e., effective linear spin–phonon coupling terms in this space) are represented by the size and directions of the arrows on the plot. The horizontal and vertical components of the arrows reflect the relative contributions to the $a_1(2)$ and $a_1(1)$ modes, respectively. It is evident from this representation that, for the D_{4h} structure, the gradient in g_z-value is small for any linear combination of these two structural coordinates. However, upon increasing the angle, α, the gradient in g_z systematically increases. This reflects the larger slope of the g_z-value vs. Cu–Cl bond length observed for D_{2d} (0.612 g_z/Å) vs. D_{4h} (0.482 g_z/Å) $[CuCl_4]^{2-}$. This map is expected to translate to any four coordinate Cu(II) complex. Indeed, previous EPR experiments on a large scope of Cu(II) complexes have concluded that spin relaxation rates are faster for tetrahedrally-distorted geometries vs. square planar geometries.[69] This observation is fully supported by extension of the model derived here (see

Figure S19).The 2D maps are also presented for spin density and the $^2B_{2g}/^2B_1$ ligand field transition energies, wherein the trends in both cases track with expressions in Section 2.1.

Individual ligand field contributions from the ligand field transition energy and spin density are given in Figures 6B and 6C, respectively. Even though the excited state linear coupling term of the $^2B_{2g}$ excited state (in D_{4h}) is larger than the $^2B_1$ state (in D_{2d}) (also compare blue lines in Figure 4A), the resultant effect on the gradient in g_z-value is smaller because the initial $^2B_{2g}$ state is higher in energy than the $^2B_1$ state. Furthermore, the effective decoherence map generated using the Cu spin density (Figure 6C) shows that the gradient of the change in absolute value of the spin density increases with increasing angle, α. This behavior is similar to Figure 6A for g_z. While it is clear that the D_{2d} structure has a larger spin–phonon coupling term in the g_z-plot alone, the different behaviors for the individual contributions from ligand field transition energy (Figure 6B) and spin density (Figure 6C) are insightful and in line with the expressions derived in Section 2.1.

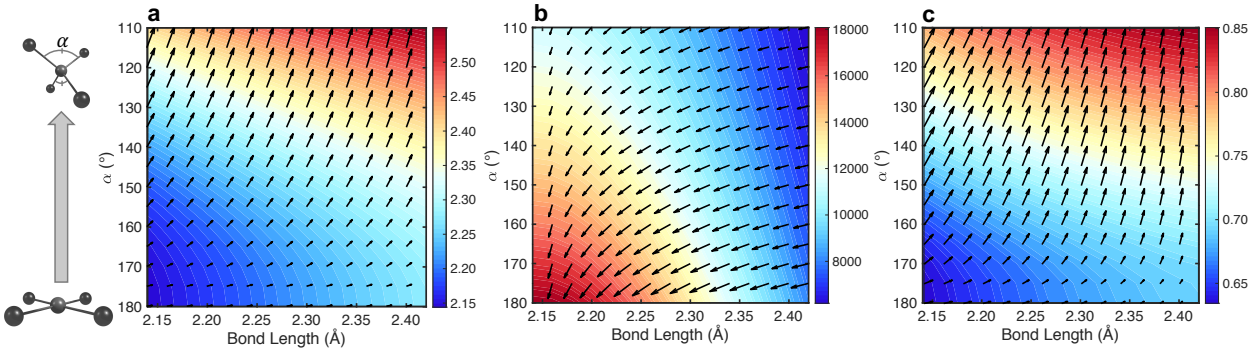

Figure 6. Effective decoherence maps generated using 225 geometries of $[CuCl_4]^{2-}$ spanning different bond lengths and angles, α, and the corresponding gradients (denoted by the size and magnitude of the arrows) in the 2D space. (a) g_z-value, (b) $^2B_{2g}/^2B_1$ ligand field energy (cm^{-1}), and (c) Loewdin spin density on Cu.

2.3. Spin–Phonon Coupling Terms in C_{4v} $[VOCl_4]^{2-}$ and Comparisons to D_{4h} $[CuCl_4]^{2-}$.

The analyses presented above for $[CuCl_4]^{2-}$ are extended to $[VOCl_4]^{2-}$. The bond metrics of the X-ray crystal structure and an idealized C_{4v} model structure are given in Table S5. As for $[CuCl_4]^{2-}$, the X-ray structure and idealized structure gave essentially identical results and only the idealized structure is considered. The DFT calculated g-values and ligand field excited state energies for C_{4v} $[VOCl_4]^{2-}$ are compared to experiment in Tables 3 and 4, respectively. Experimentally, the g_z- and $g_{x,y}$-values of $[VOCl_4]^{2-}$ are 1.948 and 1.979, respectively.[70] The calculated values are 1.963 and 1.973, respectively, in fair agreement with experiment. The HF dependence of the g_z-value for this

structure is given in Figure S13. For overall consistency and accuracy, calculations reported here for V(IV) complexes utilize 60 % HF exchange, as this value provides better overall agreement across a variety of other V(IV)-based complexes.

Table 3. Comparisons between a variety of experimental and calculated g-values for C_{4v} $[VOCl_4]^{2-}$ and other V(IV) complexes.

Molecule	g_x		g_y		g_z	
	Exp.	**Calc.**	**Exp.**	**Calc.**	**Exp.**	**Calc.**
C_{4v} $[VOCl_4]^{2-}$ [a]	1.979	1.973	1.979	1.973	1.948	1.962
C_{4v} $[VOCl_4]^{2-}$ [b]	1.979	1.973	1.979	1.973	1.948	1.963
VOPc [c]	1.989	1.973	1.989	1.973	1.966	1.963
$VO(acac)_2$ [d]	1.975	1.978	1.979	1.980	1.949	1.945
$[VO(cat)_2]^{2-}$ [e]	1.980	1.976	1.988	1.982	1.956	1.951
$[VO(dmit)_2]^{2-}$ [f]	1.986	1.979	1.988	1.977	1.970	1.963
$[V(bdt)_3]^{2-}$ [g]	1.970	1.947	1.970	1.949	1.988	1.962
$[V(bds)_3]^{2-}$ [g]	1.960	1.872	1.955	1.871	1.950	1.849

[a] Crystal structure from ref. 76, g-values from ref. 70.
[b] Idealized structure from crystal structure.
[c] DFT-Optimized structure. g-values from ref. 75.
[d] DFT-Optimized structure. g-values from ref. 77.
[e] DFT-Optimized structure. g-values from ref. 43.
[f] $VO(dmit)_2$: xtal structure and g values from ref. 53.
[g] g-values and xtal structures from ref. 33.

Table 4. Comparisons between experimental and calculated ligand field transitions for C_{4v} $[VOCl_4]^{2-}$.

Exp.[a] (cm^{-1})	**Assignment**	**Calc. (cm^{-1})[b]**	**Calc. (cm^{-1})[c]**
~12000	$^2B_2 \rightarrow {}^2B_1$	15080	15230
13700	$^2B_2 \rightarrow {}^2E$	15925	16325
		16825	16325
22000	$^2B_2 \rightarrow {}^2A_1$	29270	19190

[a] Ref. 71.
[b] X-ray crystal structure from ref. 76.
[c] Idealized structure from crystal structure.

A vibrational frequency calculation was carried out on the idealized C_{4v} $[VOCl_4]^{2-}$ structure. The energies, symmetry labels, and scaled vector displacements for all 12 normal modes of vibration are given in Table S6. Spin–phonon calculations for the g_z-value of C_{4v} $[VOCl_4]^{2-}$ are given in Figure 7A, and their fits are given in Table S7a. A strong coupling term for the g_z-value

is observed for the totally symmetric $a_1(2)$ V(IV)–Cl breathing mode (mode 9, 323 cm^{-1}). The linear fits provide slopes of 0.068 g_z/Q_i and -0.130 g_z/Å. These slopes are significantly smaller than those observed for $a_{1g}/a_1(2)$ modes of either D_{4h} (-0.241 g_z/Q_i and 0.482 g_z/Å) or D_{2d} (-0.306 g_z/Q_i and 0.612 g_z/Å) $[CuCl_4]^{2-}$. The ratios of the C_{4v} $[VOCl_4]^{2-}$ and D_{4h} $[CuCl_4]^{2-}$ slopes are ~0.27. This is very similar to the relative magnitudes of the V(IV) (250 cm^{-1}) and Cu(II) (–830 cm^{-1}) SOC constants (0.3). This shows that spin–phonon coupling terms of V(IV) are systematically decreased by a factor of ~3.3, largely due to the reduced SOC constant of V(IV) relative to Cu(II).

For C_{4v} $[VOCl_4]^{2-}$, of the other vibrations with energies less than $a_1(2)$, modes 1 ($b_1(1)$, –51 cm^{-1}), 2/3 (*e (1a, 1b)*, 160 cm^{-1}), 4 ($a_1(1)$, 166 cm^{-1}), 5 (b_2, 187 cm^{-1}), 6 ($b_1(2)$, 233 cm^{-1}), 7/8 (*e (2a, 2b)*, 267 cm^{-1}) all exhibit quadratic coupling terms. From low to high energy, the largest quadratic coupling terms are observed for modes $b_1(1)$ (-0.016 g_z/Q_i), *e(1a, 1b)* (-0.020 g_z/Q_i), $a_1(1)$ (-0.018 g_z/Q_i), $b_1(2)$ (-0.016 g_z/Q_i), and *e(2a, 2b)* (0.017 g_z/Q_i). These quadratic coefficients are significantly less than the important low-energy quadratic modes in D_{4h} $[CuCl_4]^{2-}$, which ranged from 0.056 to 0.118 g_z/Q_i. When scaled for the different SOC constant of V(IV), the quadratic coefficients for $[VOCl_4]^{2-}$ range from 0.054 to 0.067 g_z/Q_i, which are much closer to the those for D_{4h} $[CuCl_4]^{2-}$. For more direct comparison, the coefficient of the b_{2u} mode of D_{4h} $[CuCl_4]^{2-}$ is 0.063 g_z/Q_i, while for the $b_1(1)$ mode of $[VOCl_4]^{2-}$ is -0.016 g_z/Q_i. Also, the coefficient of the a_{2u} mode of D_{4h} $[CuCl_4]^{2-}$ is 0.119 g_z/Q_i, while for the $a_1(1)$ mode of $[VOCl_4]^{2-}$ is -0.018 g_z/Q_i. From group theory, these modes correlate between the D_{4h} and C_{4v} point groups. For example, the a_{2u} mode involves out-of-plane Cu motion, while the $a_1(1)$ mode involves movement of the vandyl unit out-of-plane with respect to the chloride ligands. Thus, the spin–phonon coupling terms of both linear and quadratic modes are significantly less for the vandyl complex relative to the Cu(II) complexes. Scaled for angle change, the absolute values of the b_{2u} and $b_1(1)$ slopes are 0.98 x 10^{-4} (g_z/°) and 0.28 x 10^{-4} (g_z/°), respectively, with the b_{2u} mode being larger by a factor of 3.5. Scaled for metal displacement, the absolute values of the a_{2u} and $a_1(1)$ slopes are 0.216 and 0.077 (g_z/Å), respectively, with the a_{2u} mode being larger by a factor of ~2.8. In both cases, the difference in slope is strongly influenced by the ratio of the SOC constant.

Vibrational analyses of the $^2B_1$ excited state energies were also carried out for C_{4v} $[VOCl_4]^{2-}$. Comparisons between experimental and calculated ligand field transitions are given are Table 4. Experimentally, the $^2B_1$, ^2E, and $^2A_1$ ligand field transitions of C_{4v} $[VOCl_4]^{2-}$ are observed at ~12000, 13700, and 22000 cm^{-1}, respectively.[71] The $^2B_2 \rightarrow {}^2B_1$ transition provides the SOC of

orbital angular momentum for g_z, while the $^2B_2 \rightarrow {}^2E$ transition provides SOC for $g_{x,y}$ (Figure 1). A TDDFT calculation gives the energies of these transitions at 15080 and 16325 cm^{-1}, respectively, in fairly good agreement.

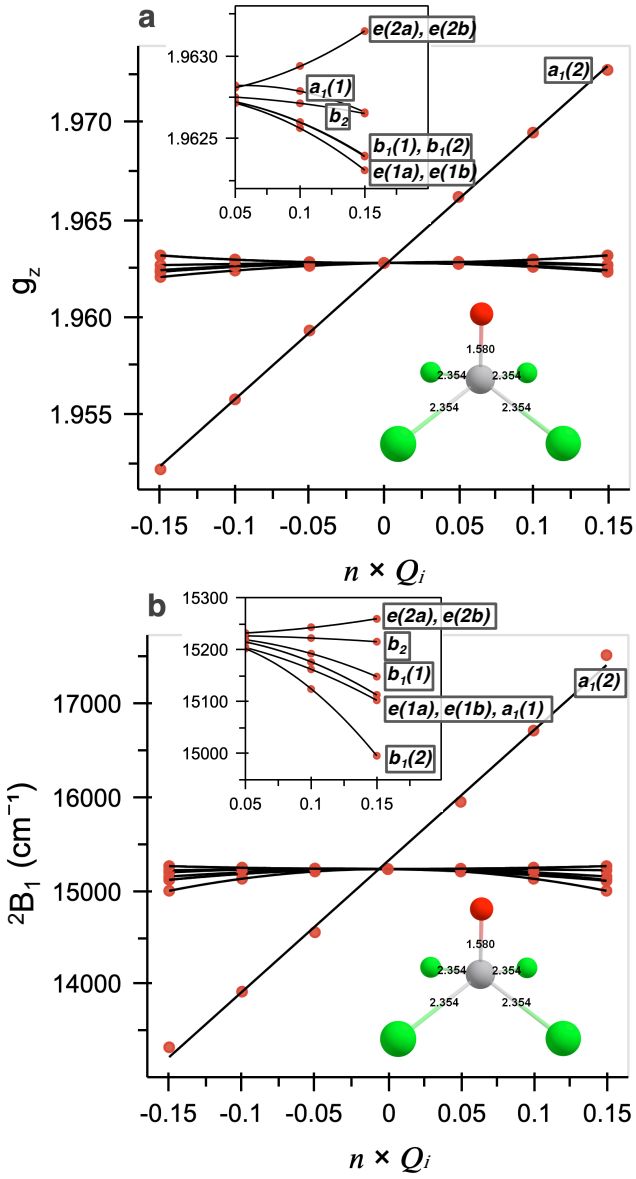

Figure 7. LFT parameters along the vibrational coordinates of the first nine vibrational modes of $[VOCl_4]^{2-}$. (a) g_z-value, (b) ligand field excited state transition energy.

The vibrational analysis of the $^2B_1$ ligand field excited state is given in Figure 8b, with fits given in Table S7a. As with the g_z-value analysis, the totally symmetric *a1(2)* mode exhibits the

largest coupling term. The slope of the $a_1(2)$ mode is 13945 cm^{-1}/Q_i (-26450 cm^{-1}/Å). These values are similar to those of D_{4h} $[CuCl_4]^{2-}$ (12405 cm^{-1}/Q_i or -24940 cm^{-1}/Å). However, despite having similar ligand field excited state energies (14475 vs. 15080 cm^{-1}) and slopes (-26450 and -24940 cm^{-1}/Å) for the totally symmetric stretch, the corresponding slopes for the change in g_z-value are significantly lower for $[VOCl_4]^{2-}$ vs. $[CuCl_4]^{2-}$ (-0.130 g_z/Å vs. 0.482 g_z/Å, respectively). This difference is due to the different ratio of SOC constants for V(IV) and Cu(II).

The total Loewdin unoccupied V(IV) d(xy) character and V(IV) spin density for $[VOCl_4]^{2-}$ are 88 % and 0.98, respectively. As expected, the covalency of the V(IV)–Cl bonds are significantly lower than those of D_{4h} $[CuCl_4]^{2-}$ (e.g., 88 % vs. 65 % unoccupied metal d character). The spin density vibrational analysis for C_{4v} $[VOCl_4]^{2-}$ is given in Figure S14, with fits given in Table S7e. The fits for the $a_1(2)$ mode give values of -0.102 SD/Q_i and 0.194 SD/Å. These values are smaller than those observed for D_{4h} $[CuCl_4]^{2-}$ (-0.157 SD/Q_i and 0.221 SD/Å), consistent with the σ overlap in $[CuCl_4]^{2-}$ (Figure 1). The spin density change for $[VOCl_4]^{2-}$ is due to the π-type interaction between the out-of-plane Cl p orbitals and the V d(xy) orbital.

The spin–phonon coupling terms for the $g_{x,y}$-values for the C_{4v} structure are given in Figure S15, with the corresponding fits given in Table S7b and S7c. Both g_x and g_y give similar results, and only g_x is considered. As observed for D_{4h} $[CuCl_4]^{2-}$, the spin–phonon coupling terms are different in the $g_\perp$ region relative to $g_\parallel$. For the most part, the magnitudes of the spin–phonon coupling terms are decreased going from $g_\parallel$ to $g_\perp$. For instance, the slope of the $a_1(2)$ mode decreases from 0.068 to 0.005 g_z/Q_i, and the slopes of the $b_1(1)$ and $a_1(1)$ modes go from -0.016 and -0.018 g_z/Q_i to -0.002 and -0.007 g_z/Q_i, respectively. The b_2 and $e(2a, 2b)$ modes exhibit an increase in coupling term (0.017 to -0.032 g_z/Q_i). These changes in spin–phonon coupling terms are correlated to the changes in the slopes of the ligand field transitions. The vibrational analyses of the ^2E ligand field excited state energies are given in Figure S16. For instance, for the b_2 mode, the excited state slope changes from -565 to 3775 cm^{-1}/Q_i. For the $e(2a, 2b)$ modes, the slopes go from 1370 to -5945/-9620 cm^{-1}/Q_i.

In summary, the totally symmetric $a_1(2)$ mode exhibits a strong spin–phonon coupling term for C_{4v} $[VOCl_4]^{2-}$. This makes for an insightful comparison to the a_{1g} mode of D_{4h} $[CuCl_4]^{2-}$. The magnitude of the spin–phonon coupling term is significantly less for $[VOCl_4]^{2-}$. This difference in spin–phonon coupling terms could be quantified to a factor of ~0.27, which is ascribed here to the difference in SOC constants for V(IV) vs. Cu(II). Importantly, $[VOCl_4]^{2-}$ and $[CuCl_4]^{2-}$ have

similar ligand field excited state energies and similar excited state coupling terms, and $[VOCl_4]^{2-}$ has a smaller slope in covalency, which is due to different relative orbital overlaps for the two complexes. These observations further support that the reduced SOC constant reduces the spin–phonon coupling terms. Also, as observed for $[CuCl_4]^{2-}$, the spin–phonon coupling terms in $[VOCl_4]^{2-}$ are anisotropic, with different modes being activated in the $g_{\parallel}$ and $g_{\perp}$ regions. Nonetheless, the spin–phonon coupling terms of $[VOCl_4]^{2-}$, even when scaled for degree of distortion, are significantly reduced relative to $[CuCl_4]^{2-}$ in either $g_{\parallel}$ and $g_{\perp}$ directions. The reduced spin–phonon coupling terms will play a major role in the room temperature coherence properties of vanadyl complexes relative to Cu(II) complexes.

3. Discussion.

Transition metal complexes are being explored as qubits for quantum computing. In addition to significant hurdles related to the eventual quantum entanglement of molecular qubits, spin–phonon coupling in transition metal complexes often prohibits the observation of room temperature coherence properties. This has inspired resent research efforts to better understand the nature of spin–phonon coupling in transition metal complexes and how it might be tuned and controlled by variations in the ligand set and thus the ligand field environment.[13–15,33,44] As highlighted in the Introduction, spin–phonon couplings also play important roles in single molecule magnets and photophysics, and studies directed at fundamental understanding will have broad impact.

Above, we have outlined a general LFT model of spin–phonon coupling terms in S = ½ transition metal complexes. This model is derived from the first and second derivatives of the LFT expressions of g-values given in Section 2.1.[54] While these expressions define the zero temperature magnitudes of spin–phonon coupling terms in S = ½ complexes, they can be expanded to consider additional dynamic effects through the variance of g_z, $\langle g_z^2 \rangle$, which highlights the importance of the first derivative, $\frac{\partial g_z}{\partial Q_i}$, and therefore its role in the coherence lifetimes of S = ½ transition metal complexes. This suggests that, without considering thermal population, odd modes such as totally symmetric stretches will have a more substantial effect on spin-phonon coupling terms and decoherence compared to even modes, in which their value of relevance, $\frac{\partial^2 g_z}{\partial Q_i^2}$, only appears in the second order term of the Taylor expansion (equation 5). The fundamental behavior of these expressions were borne out by an extensive range of DFT and TD-DFT calculations on

minimalistic S = ½ models, D_{4h}/D_{2d} $[CuCl_4]^{2-}$ and C_{4v} $[VOCl_4]^{2-}$. Together, the results above provide a general description of the roles of transition metal geometric and electronic structure in spin–phonon coupling. For instance, the magnitudes of spin–phonon coupling terms are strongly influenced by excited state SOC of orbital angular momentum into the ground state and are predicted to be strongly influenced by the energy of the particular ligand field excited state mixing with the ground state (equations 6 and 7) (e.g., $^2B_{2g}$ for a $^2B_{1g}$ ground state in D_{4h} $[CuCl_4]^{2-}$). This excited state SOC contribution is governed by the ligand field geometry about the metal complex. For example, going from D_{4h} to D_{2d} $[CuCl_4]^{2-}$ turns on additional mode coupling terms due to the enhancement of excited state coupling terms (Figure 4). Furthermore, the magnitude of spin–phonon coupling terms are strongly influenced by the covalency of ligand–metal bonds. This dynamic effect largely reflects a relativistic nephelauxetic effect, which effectively modulates the SOC constant of the metal from that of the free ion. In short, the more covalent the ligand–metal bond, the smaller the spin–phonon coupling terms become. Relatedly, a significant overall reduction in SOC constant can of course be achieved through the use of different transition metal complexes (e.g., V(IV) vs. Cu(II) vs. Cr(V)). As shown below, V(IV), which has a significantly lower SOC constant than Cu(II), can still maintain favorable spin–phonon coupling terms despite having significantly more ionic ligand-metal bonds than Cu(II) complexes. Complications can also arise from trying to quantify spin–phonon coupling terms in different ligand field environments, as the nature of the modes can change. However, this can be facilitated to some degree by leveraging specific group theoretical correlations as demonstrated here for D_{4h}, D_{2d}, and C_{4v} transition metal complexes. The spin–phonon analyses presented above for $[CuCl_4]^{2-}$ and $[VOCl_4]^{2-}$ are now extended to a range of S = ½ Cu(II) and V(IV) molecular qubit candidates.

3.1 Extension to Cu(II)- and V(IV)-Based Qubits.

The spin–phonon analyses of the Cu(II) qubit complexes and their g_z-values are given in Figures S17(a-d) and Tables S8(a-d). The spin-phonon analyses of the V(IV) complexes and their g_z-values for all modes up to at least 400 cm^{-1} in energy are given in Figures S18(a-f) and Tables S9(a-f). Comparisons between all geometry optimized and crystal structures are given in Tables S10(a,b) and S11(a-c) for Cu(II) and V(IV) complexes, respectively. Providing quantitative comparisons between the spin–phonon analyses for different complexes is a complicated task. This is largely because the nature and amount of atomic motions are not necessarily conserved over all vibrations.

However, as discussed here, the modes identified above for D_{4h} $[CuCl_4]^{2-}$ and C_{4v} $[VOCl_4]^{2-}$ that exhibited particularly large spin–phonon coupling terms are also those that exhibit spin–phonon coupling terms in the qubits. Thus, the parent vibrational modes provide a means to make quantitative comparisons across Cu(II) and V(IV) complexes.

Table 5. Spin–vibrational coupling terms, excited state energies, and covalencies across a variety of Cu(II) complexes/qubits.

Complex	a_{1g} (cm^{-1})	(g/Å)	a_{2u} (cm^{-1})	(g/Å)	ES[a]	M(d)[b]	M SD
D_{4h} $[CuCl_4]^{2-}$	296.3	0.482	140.5	0.216	14475	65 %	0.670
D_{2d} $[CuCl_4]^{2-}$	316.7	0.612	66.9	0.529	10440	70 %	0.760
CuPc	259.4	0.464	151.7	0.151	22165	72 %	0.734
$Cu(mnt)_2$	303.4	0.384	141.2	0.102	22305	42 %	0.434
$Cu(bdt)_2$	387.4	0.232	85.1	0.103	29700	41 %	0.424
$Cu(bds)_2$	199.3	0.165	97.8	0.039	24390	37 %	0.377

[a] Excited state which spin orbit couples into the ground state for g_z.
[b] M(d) character in unoccupied component orbital from Loewdin population analyses.
[c] Loewdin metal spin density.

The experimental and calculated g-values of Cu(II) qubits are given in Table 1,[14,33,72,73] while spin–phonon linear coupling terms and additional computational results are given in Table 5. Note X-ray crystal structures were utilized for $[Cu(mnt)_2]^{2-}$, $[Cu(bdt)_2]^{2-}$, and $[Cu(bds)_2]^{2-}$ (bds = benzene-1,2-diselenate) complexes, as their structures were not well reproduced using DFT geometry optimization. However, CuPc provided a good agreement and thus the optimized structure is used. As outlined above, the totally symmetric stretch (a_{1g} in D_{4h} $[CuCl_4]^{2-}$) and the out-of-plane motion of the metal/vanadyl moiety (a_{2u} in D_{4h} $[CuCl_4]^{2-}$ and $a_1(1)$ in C_{4v} $[VOCl_4]^{2-}$) were the main modes to consider. The nature of these modes are well conserved over the complexes considered in Tables 5 and 6 and allow for the spin–phonon coupling terms to be compared on a $Å^{-1}$ scale. As elucidated above, the linear coupling terms for the totally symmetric modes of D_{4h} and D_{2d} $[CuCl_4]^{2-}$ were determined to be 0.482 and 0.612 g_z/Å. These modes for qubit candidates CuPc,[74] $Cu(mnt)_2$,[50] $Cu(bdt)_2$,[33] and $Cu(bds)_2$[33] are 0.464, 0.384, 0.232, and 0.165 g_z/Å, respectively. Interestingly, of these qubits, $Cu(bdt)_2$ exhibited spin echoes that persist to room temperature, and it has one of the lowest spin–phonon coupling terms of the Cu(II) complexes, with only $Cu(bds)_2$ being lower. Note the lack of spin echoes for $Cu(bds)_2$ and its comparison to $Cu(bdt)_2$ is discussed further below. For the a_{2u} parent mode, the quadratic

coefficients for D_{4h} and D_{2d} $[CuCl_4]^{2-}$ were determined to be 0.216 and 0.529 g_z/Å, respectively. In a similar fashion to the a_{1g} parent mode, the quadratic coefficients of the a_{2u} parent mode decrease to 0.151, 0.102, 0.103, and 0.039 g_z/Å for CuPc, $Cu(mnt)_2$, $Cu(bdt)_2$, and $Cu(bds)_2$, respectively. Thus, there is a systematic decrease in the spin–phonon coupling terms across these Cu(II) complexes. These observations can be understood utilizing the LFT model outlined above. For example, $Cu(bdt)_2$ exhibits the highest calculated ligand field excited state energy (29700 cm^{-1}) and has highly covalent ligand–metal bonds (41 % Cu(d)). The decreased slope of $Cu(bds)_2$ is due to the increased covalency of the Cu–Se vs. Cu–S bonds (Table 5). Furthermore, the slopes and quadratic coefficients of $Cu(mnt)_2$ are larger than those $Cu(bdt)_2$ and $Cu(bds)_2$. From Table 5, this is largely reflected by the lower excited state energy (22305 cm^{-1}) (and thus the higher amount of ground state orbital angular momentum) and, to a smaller extent, the lower covalency (42 % Cu(d)). The slopes and coefficients for CuPc are increased further relative to the other Cu(II) complexes, as the Cu–N bonds are significantly more ionic than the Cu–S bonds of $Cu(mnt)_2$, $Cu(bdt)_2$ and $Cu(bds)_2$.

These electronic differences between $Cu(bdt)_2$ and $Cu(mnt)_2$ can be understood from their X-ray crystal structures. For example, the Cu–S bond lengths of $Cu(mnt)_2$ are ~2.33 Å, which are longer than those for the $Cu(bdt)_2$ complex (~2.15 Å). For $Cu(bdt)_2$, the contraction of the ligand–metal bonds destabilizes the Cu $d(x^2\text{-}y^2)$ β-LUMO orbital, which increases the energy of the $^2B_{2g}$ ligand field transition and increases the orbital overlap (covalency) of the ligand–metal bonds (Figure 1). Thus, the ligand set and $Cu(bdt)_2$ complex exhibits the ideal characteristics for a Cu(II)-based qubit. Also, while the slopes of the $Cu(bds)_2$ complex would suggest longer coherence times, the lack of spin echoes at higher temperatures can be attributed to the significant decrease in the vibrational frequency of the a_{1g} parent mode due to the mass effect of the S to Se conversion (e.g., 387 vs. 199 cm^{-1}, respectively). Interestingly, the fits to the temperature dependence of the T_1 for these complexes suggest local mode contributions of 488 ± 72 and 344 ± 80 cm^{-1}. Combined with the computational results here, these frequencies and their differences provide strong evidence that the totally symmetric a_{1g} parent mode contributes to the coherence times of Cu(II) complexes. Thus, we propose that the rapidly accessible data in Table 5 can be computed to qualitatively and semi-quantitatively evaluate and screen potential Cu(II)-based qubits.

Recent work by Sessoli et al.[13,53] has highlighted the important role of the vanadyl moiety in V(IV)-based qubits. The calculated and experimental g-values of a variety of vandyl and V(IV)

qubits are given in Table 3.[43,53,70,75–77] Their spin–phonon analyses are given in Figures S18(a-f) and Tables S9(a-f), and specific spin–phonon slopes and additional computational results are given in Table 6. Note, of the vandyl complexes considered here, VOPc, $VO(acac)_2$, and $[VO(cat)_2]^{2-}$ were geometry optimized. Similarly to the Cu complexes considered above, X-ray crystal structures were used for structures where geometry optimizations resulted in significantly different structures (e.g., $[VO(dmit)_2]^{2-}$, $[V(bdt)_3]^{2-}$, and $[V(bds)_3]^{2-}$). Experimentally, long coherence times have been observed for a variety of vandyl complexes. However, only VOPc has been directly studied in a solid diamagnetic matrix, which has thus far prohibited further investigation of vanadyl complexes up to room temperature. From the data given in Table 6, there are currently no clear defining characteristics to be observed across the vanadyl complexes. Thus, other vandyl complexes, when isolated in similar solid diamagnetic matrices, will likely exhibit long relaxation times, with the potential for room temperature coherence.

The spin–phonon model presents a stark difference for vanadyl vs. six coordinate V(IV) complexes. As shown in Sessoli et al.,[13,53] six coordinate V(IV) complexes do not exhibit long T_1s at elevated temperatures. Very recently, Albino et al.[13] pointed to the role of increased excited state SOC in six coordinate complexes relative to vanadyl complexes. Furthermore, Fataftah et al.[33] compared six coordinate V(IV) complexes to Cu(II) complexes to suggest the role of increased covalency in elongating T_1 relaxation lifetimes. Here we have extended our LFT model to the $V(bdt)_3$ and $V(bds)_3$ complexes studied by Fataftah et al.[33] (Table 6). Interestingly, as pointed out by Albino et al.[13] for other six coordinate V(IV) complexes, the $V(bdt)_3$ and $V(bds)_3$ complexes exhibit very low energy calculated ligand field transitions (7935 and 6785 cm^{-1}, respectively). Furthermore, the totally symmetric stretches of these complexes were computed at 351.7 and 209.8 cm^{-1}, respectively. These modes allow for a quantitative comparison between the linear spin–phonon coupling term of Cu(II) complexes on a $Å^{-1}$ scale. The linear coupling terms for $V(bds)_6$ in the $g_{\|}$ and $g_{\perp}$ regions are -0.420 and -0.357 g/Å, respectively. For comparison, the linear coupling term of the totally symmetric a_{1g} parent mode of $Cu(bdt)_2$ is smaller (0.232 g_z/Å). Also, the calculated vibrational frequency decreases and the linear coupling terms increase going from $V(bdt)_3$ to $V(bds)_3$. Thus, the longer spin–lattice relaxation time at higher temperatures for $Cu(bdt)_2$ vs. $V(bdt)_3$ is not due to differences in ligand–metal covalency, but rather stems from efficient excited state SOC as a result of the relatively low energy ligand field transition energies for $V(bdt)_3$. This is further supported by the observation of room temperature coherence in vanadyl

complexes,[37] despite ionic ligand metal bonding. Together, these DFT/TDDFT calculations are consistent with the LFT model derived here and further highlight the importance of considering both excited state SOC and ligand–metal covalency when comparing different complexes with different metals and/or coordination environments.

Table 6. Spin–vibrational coupling terms across a variety of V(IV) complexes.

Complex	**Mode (cm^{-1})**	**(g_z/Q_i)**	**ES[a]**	**M(d)[b]**	**M SD**
C_{4v} $[VOCl_4]^{2-}$	166.4	-0.018	15230	88 %	0.983
	323.5	0.068			
	394.9	-0.313			
	394.9	-0.322			
VOPc	177.3	-0.009	22745	85 %	0.985
	260.0	-0.006			
	317.3	-0.014			
	384.2	-0.063			
	384.2	-0.059			
	393.9	-0.017			
$VO(acac)_2$	192.3	0.006	17955	84 %	0.972
	277.6	0.006			
	295.6	-0.021			
	374.5	-0.029			
	391.0	-0.030			
	475.4	0.022			
$VO(cat)_2$	186.1	-0.004	19335	65 %	0.987
	280.9	-0.017			
	366.3	-0.012			
	388.4	-0.039			
	437.4	-0.066			
$VO(dmit)_2$	116.8	-0.003	20120	50 %	0.999
	178.6	-0.016			
	350.7	-0.053			
	378.5	0.031			
	414.0	-0.022			
	426.6	-0.058			
Complex	**Mode (cm^{-1})**	**($g_{\|\|}$/Å)**	**($g_{\perp}$/Å)**	**ES**	
$V(bdt)_3$	351.7	-0.420	-0.357	7935	

$V(bds)_3$	209.8	-1.744	-0.766	6785	

[a] Excited state which spin orbit coupling into the ground state.
[b] M(d) character in unoccupied component orbital from Loewdin population analyses.
[c] Loewdin metal spin density.

3.2 Ligand Field Strain in Qubits.

As previously highlighted for D_{4h}/D_{2d} $[CuCl_4]^{2-}$, the planar D_{4h} Cu(II) structure represents a saddle point on the ground state potential energy surface that can only be stabilized in the presence of crystal packing forces.[57,58] The formation of this structure in $[CuCl_4]^{2-}$ was likened to the entatic/rack state in bioinorganic chemistry, where the protein architecture (inclusive of first and second sphere contributions, as well as long range H-bonding and electrostatics) can place a metal ion in a strained ligand field.[78–81] This ligand field strain can generate unique properties. The entatic/rack state and ligand field strain is therefore of relevance to molecular qubits. For example, Cu(II)-based complexes with the longest coherence times are square planar Cu(II) sites stabilized in diamagnetic lattices (e.g., $Cu(mnt)_2$[50] and $Cu(bdt)_2$[33]). The geometric dependence to T_1 was also noted in an EPR study of a variety of Cu(II) complexes.[69] Here we have shown that the origin of this dependence for the square planar Cu(II) geometry derives from the significant minimization of excited state coupling terms, which reduces dynamic SOC of orbital angular momentum into the ground state (Figure 4).

In addition to crystal packing forces, variations in the ligand set can effectively control the deviation from planarity in Cu(II) complexes. This can be observed directly in the dependence of the electronic energy as a function of the b_{2u} parent mode (in D_{4h}) distortion. For instance, as noted above, distortion along this mode will decrease the energy for the square planar Cu(II) complexes studied here, which results in the b_{2u} mode being imaginary. However, this is not the case for CuPc. Thus, linking the four N-based ligands into the aromatic planar structure of the Pc ligand provides an entatic state that can oppose distortions along the b_{2u} parent mode. However, the drawback of the Pc ligand arises also from its N-based coordination, which gives rise to fairly ionic ligand–metal bonds and opposes the effects provided by the rigid and constrained ligand field (i.e., entatic state).

In relation, significant efforts have been guided toward better identifying, understanding, and quantifying entatic states,[82–84] which have traditionally been used to rationalize electron transfer properties. However, given the general nature of this description, it is being extended to

other scenarios, including photochemistry and catalysis.[85–89] Strain effects have also been discussed in the context of both ground and excited states and their contributions to the coherence properties in solid state qubits (e.g, vacancies in diamond).[10–12,90] Thus, engineering ligand field strain and rigidity into covalent environments will be useful for advancing the geometric and electronic structural contributions to the quantum coherence of transition metal complexes, and the model outlined here can guide these future investigations.

4. Conclusion.

The spin–phonon coupling terms of minimalized D_{4h}/D_{2d} $[CuCl_4]^{2-}$ and C_{4v} $[VOCl_4]^{2-}$ complexes translate onto Cu(II)- and V(IV)-based molecular qubits and are dominated by three major factors: 1) the magnitude of the metal-based SOC constant, 2) the initial magnitude and gradient of change in ground state orbital angular momentum, which is governed by the ligand field excited state energies, and 3) dynamic relativistic nephelauxetic contributions, including the initial magnitude and gradient in the covalency of the ligand–metal bonds. Factors 1) and 3) are directly related, as covalency further reduces the SOC constant of a metal in a complex relative to that of the free ion. LFT expressions derived here predict spin–phonon coupling terms in both odd and even modes are important to consider for decoherence times (equation 5). However, odd modes such as the totally symmetric stretch play a key role for decoherence times. We have further shown how the LFT expressions and thus spin–phonon coupling terms (equations 6 and 7) can be directly related to spectroscopic observables and calculable quantities. For Cu(II), key geometric and symmetry factors, including ligand field strain, significantly lower excited state coupling terms while simultaneously increasing orbital overlap and ligand–metal covalency. Importantly, all factors relating to excited state SOC and covalency need to be evaluated when comparing spin–phonon coupling terms, including local mode contributions to T_1 and T_m relaxation times, of various metal complexes. The model outlined here provides a means to quantify spin–phonon coupling terms for given vibrational modes for any S = ½ molecule, providing a powerful means to benchmark current and future qubit candidates. The further discovery of room temperature coherent materials will provide exciting opportunities to develop fundamental structure-function correlations for spin–phonon coupling in transition metal complexes.

Acknowledgments.

We acknowledge Prof. Edward Solomon, Dr. Alec Follmer, Roman Korol, and Nicholas Higdon for helpful discussions. Financial support from Caltech and the Dow Next Generation Educator Fund is gratefully acknowledged.

References.

1. T. J. Penfold, E. Gindensperger, C. Daniel and C. M. Marian, *Chem. Rev.*, 2018, **118**, 6975–7025.
2. K. S. Kjær, T. B. V. Driel, T. C. B. Harlang, K. Kunnus, E. Biasin, K. Ledbetter, R. W. Hartsock, M. E. Reinhard, S. Koroidov, L. Li, M. G. Laursen, F. B. Hansen, P. Vester, M. Christensen, K. Haldrup, M. M. Nielsen, A. O. Dohn, M. I. Pápai, K. B. Møller, P. Chabera, Y. Liu, H. Tatsuno, C. Timm, M. Jarenmark, J. Uhlig, V. Sundstöm, K. Wärnmark, P. Persson, Z. Németh, D. S. Szemes, É. Bajnóczi, G. Vankó, R. Alonso-Mori, J. M. Glownia, S. Nelson, M. Sikorski, D. Sokaras, S. E. Canton, H. T. Lemke and K. J. Gaffney, *Chem. Sci.*, 2019, **10**, 5749–5760.
3. H. T. Lemke, K. S. Kjær, R. Hartsock, T. B. van Driel, M. Chollet, J. M. Glownia, S. Song, D. Zhu, E. Pace, S. F. Matar, M. M. Nielsen, M. Benfatto, K. J. Gaffney, E. Collet and M. Cammarata, *Nat. Commun.*, 2017, **8**, 15342.
4. R. Monni, G. Auböck, D. Kinschel, K. M. Aziz-Lange, H. B. Gray, A. Vlček and M. Chergui, *Chem. Phys. Lett.*, 2017, **683**, 112–120.
5. M. Pižl, B. M. Hunter, G. M. Greetham, M. Towrie, S. Záliš, H. B. Gray and A. Vlček, *J. Phys. Chem. A*, 2017, **121**, 9275–9283.
6. A. Lunghi, F. Totti, S. Sanvito and R. Sessoli, *Chem. Sci.*, 2017, **8**, 6051–6059.
7. A. Lunghi, F. Totti, R. Sessoli and S. Sanvito, *Nat. Commun.*, 2017, **8**, 14620.
8. D. H. Moseley, S. E. Stavretis, K. Thirunavukkuarasu, M. Ozerov, Y. Cheng, L. L. Daemen, J. Ludwig, Z. Lu, D. Smirnov, C. M. Brown, A. Pandey, A. J. Ramirez-Cuesta, A. C. Lamb, M. Atanasov, E. Bill, F. Neese and Z.-L. Xue, *Nat. Commun.*, 2018, **9**, 2572.
9. M. Atanasov and F. Neese, *J. Phys. Conf. Ser.*, 2018, **1148**, 012006.
10. P. Udvarhelyi, V. O. Shkolnikov, A. Gali, G. Burkard and A. Pályi, *Phys. Rev. B*, 2018, **98**, 075201.
11. M. L. Goldman, A. Sipahigil, M. W. Doherty, N. Y. Yao, S. D. Bennett, M. Markham, D. J. Twitchen, N. B. Manson, A. Kubanek and M. D. Lukin, *Phys. Rev. Lett.*, 2015, **114**, 145502.
12. M. L. Goldman, M. W. Doherty, A. Sipahigil, N. Y. Yao, S. D. Bennett, N. B. Manson, A. Kubanek and M. D. Lukin, *Phys. Rev. B*, 2015, **91**, 165201.
13. A. Albino, S. Benci, L. Tesi, M. Atzori, R. Torre, S. Sanvito, R. Sessoli and A. Lunghi, *Inorg. Chem.*, 2019, **58**, 10260–10268.
14. L. Escalera-Moreno, N. Suaud, A. Gaita-Ariño and E. Coronado, *J. Phys. Chem. Lett.*, 2017, **8**, 1695–1700.
15. L. Escalera-Moreno, J. J. Baldoví, A. Gaita-Ariño and E. Coronado, *Chem. Sci.*, 2018, **9**, 3265–3275.
16. V. v. Dobrovitski, G. d. Fuchs, A. l. Falk, C. Santori and D. d. Awschalom, *Annu. Rev. Condens. Matter Phys.*, 2013, **4**, 23–50.
17. D. I. Khomskii and G. A. Sawatzky, *Solid State Commun.*, 1997, **102**, 87–99.
18. J. Orenstein and A. J. Millis, *Science*, 2000, **288**, 468–474.

19. A. Lanzara, P. V. Bogdanov, X. J. Zhou, S. A. Kellar, D. L. Feng, E. D. Lu, T. Yoshida, H. Eisaki, A. Fujimori, K. Kishio, J.-I. Shimoyama, T. Noda, S. Uchida, Z. Hussain and Z.-X. Shen, *Nature*, 2001, **412**, 510–514.
20. Y. Tokura and N. Nagaosa, *Science*, 2000, **288**, 462–468.
21. M. Mochizuki, N. Furukawa and N. Nagaosa, *Phys. Rev. B*, 2011, **84**, 144409.
22. T. V. Brinzari, J. T. Haraldsen, P. Chen, Q.-C. Sun, Y. Kim, L.-C. Tung, A. P. Litvinchuk, J. A. Schlueter, D. Smirnov, J. L. Manson, J. Singleton and J. L. Musfeldt, *Phys. Rev. Lett.*, 2013, **111**, 047202.
23. M. Rini, R. Tobey, N. Dean, J. Itatani, Y. Tomioka, Y. Tokura, R. W. Schoenlein and A. Cavalleri, *Nature*, 2007, **449**, 72–74.
24. D. Fausti, R. I. Tobey, N. Dean, S. Kaiser, A. Dienst, M. C. Hoffmann, S. Pyon, T. Takayama, H. Takagi and A. Cavalleri, *Science*, 2011, **331**, 189–191.
25. M. Först, C. Manzoni, S. Kaiser, Y. Tomioka, Y. Tokura, R. Merlin and A. Cavalleri, *Nat. Phys.*, 2011, **7**, 854–856.
26. S. F. Maehrlein, I. Radu, P. Maldonado, A. Paarmann, M. Gensch, A. M. Kalashnikova, R. V. Pisarev, M. Wolf, P. M. Oppeneer, J. Barker and T. Kampfrath, *Sci. Adv.*, 2018, **4**, eaar5164.
27. D. P. DiVincenzo, *Fortschritte Phys.*, 2000, **48**, 771–783.
28. J. M. Zadrozny, J. Niklas, O. G. Poluektov and D. E. Freedman, *ACS Cent. Sci.*, 2015, **1**, 488–492.
29. J. M. Zadrozny, J. Niklas, O. G. Poluektov and D. E. Freedman, *J. Am. Chem. Soc.*, 2014, **136**, 15841–15844.
30. M. S. Fataftah, J. M. Zadrozny, S. C. Coste, M. J. Graham, D. M. Rogers and D. E. Freedman, *J. Am. Chem. Soc.*, 2016, **138**, 1344–1348.
31. M. S. Fataftah, S. C. Coste, B. Vlaisavljevich, J. M. Zadrozny and D. E. Freedman, *Chem. Sci.*, 2016, **7**, 6160–6166.
32. M. J. Graham, J. M. Zadrozny, M. Shiddiq, J. S. Anderson, M. S. Fataftah, S. Hill and D. E. Freedman, *J. Am. Chem. Soc.*, 2014, **136**, 7623–7626.
33. M. S. Fataftah, M. D. Krzyaniak, B. Vlaisavljevich, M. R. Wasielewski, J. M. Zadrozny and D. E. Freedman, *Chem. Sci.*, , DOI:10.1039/C9SC00074G.
34. T. J. Pearson, D. W. Laorenza, M. D. Krzyaniak, M. R. Wasielewski and D. E. Freedman, *Dalton Trans.*, 2018, **47**, 11744–11748.
35. J. M. Zadrozny, A. T. Gallagher, T. D. Harris and D. E. Freedman, *J. Am. Chem. Soc.*, 2017, **139**, 7089–7094.
36. C.-J. Yu, M. D. Krzyaniak, M. S. Fataftah, M. R. Wasielewski and D. E. Freedman, *Chem. Sci.*, , DOI:10.1039/C8SC04435J.
37. M. Atzori, L. Tesi, E. Morra, M. Chiesa, L. Sorace and R. Sessoli, *J. Am. Chem. Soc.*, 2016, **138**, 2154–2157.
38. T. Yamabayashi, M. Atzori, L. Tesi, G. Cosquer, F. Santanni, M.-E. Boulon, E. Morra, S. Benci, R. Torre, M. Chiesa, L. Sorace, R. Sessoli and M. Yamashita, *J. Am. Chem. Soc.*, 2018, **140**, 12090–12101.
39. L. Tesi, E. Lucaccini, I. Cimatti, M. Perfetti, M. Mannini, M. Atzori, E. Morra, M. Chiesa, A. Caneschi, L. Sorace and R. Sessoli, *Chem. Sci.*, 2016, **7**, 2074–2083.
40. L. Tesi, A. Lunghi, M. Atzori, E. Lucaccini, L. Sorace, F. Totti and R. Sessoli, *Dalton Trans.*, 2016, **45**, 16635–16643.

41. D. Stinghen, M. Atzori, C. M. Fernandes, R. R. Ribeiro, E. L. de Sá, D. F. Back, S. O. K. Giese, D. L. Hughes, G. G. Nunes, E. Morra, M. Chiesa, R. Sessoli and J. F. Soares, *Inorg. Chem.*, 2018, **57**, 11393–11403.
42. M. Atzori, A. Chiesa, E. Morra, M. Chiesa, L. Sorace, S. Carretta and R. Sessoli, *Chem. Sci.*, 2018, **9**, 6183–6192.
43. M. Atzori, S. Benci, E. Morra, L. Tesi, M. Chiesa, R. Torre, L. Sorace and R. Sessoli, *Inorg. Chem.*, 2018, **57**, 731–740.
44. M. Atzori, L. Tesi, S. Benci, A. Lunghi, R. Righini, A. Taschin, R. Torre, L. Sorace and R. Sessoli, *J. Am. Chem. Soc.*, 2017, **139**, 4338–4341.
45. A. Ardavan, A. M. Bowen, A. Fernandez, A. J. Fielding, D. Kaminski, F. Moro, C. A. Muryn, M. D. Wise, A. Ruggi, E. J. L. McInnes, K. Severin, G. A. Timco, C. R. Timmel, F. Tuna, G. F. S. Whitehead and R. E. P. Winpenny, *Npj Quantum Inf.*, 2015, **1**, 15012.
46. E. Garlatti, T. Guidi, S. Ansbro, P. Santini, G. Amoretti, J. Ollivier, H. Mutka, G. Timco, I. J. Vitorica-Yrezabal, G. F. S. Whitehead, R. E. P. Winpenny and S. Carretta, *Nat. Commun.*, 2017, **8**, 14543.
47. G. A. Timco, S. Carretta, F. Troiani, F. Tuna, R. J. Pritchard, C. A. Muryn, E. J. L. McInnes, A. Ghirri, A. Candini, P. Santini, G. Amoretti, M. Affronte and R. E. P. Winpenny, *Nat. Nanotechnol.*, 2009, **4**, 173–178.
48. J. Ferrando-Soria, S. A. Magee, A. Chiesa, S. Carretta, P. Santini, I. J. Vitorica-Yrezabal, F. Tuna, G. F. S. Whitehead, S. Sproules, K. M. Lancaster, A.-L. Barra, G. A. Timco, E. J. L. McInnes and R. E. P. Winpenny, *Chem*, 2016, **1**, 727–752.
49. J. McGuire, H. N. Miras, J. P. Donahue, E. Richards and S. Sproules, *Chem. – Eur. J.*, 2018, **24**, 17598–17605.
50. K. Bader, D. Dengler, S. Lenz, B. Endeward, S.-D. Jiang, P. Neugebauer and J. van Slageren, *Nat. Commun.*, 2014, **5**, 5304.
51. K. N. Shrivastava, *Phys. Status Solidi B*, 1983, **117**, 437–458.
52. K. N. Shrivastava, *J. Phys. C Solid State Phys.*, 1982, **15**, 3869–3876.
53. M. Atzori, E. Morra, L. Tesi, A. Albino, M. Chiesa, L. Sorace and R. Sessoli, *J. Am. Chem. Soc.*, 2016, **138**, 11234–11244.
54. E. I. Solomon, *Comments Inorg. Chem.*, 1984, **3**, 225-320.
55. F. Neese, *Wiley Interdiscip. Rev. Comput. Mol. Sci.*, 2012, **2**, 73–78.
56. F. Neese, *Wiley Interdiscip. Rev. Comput. Mol. Sci.*, 2018, **8**, e1327.
57. R. K. Szilagyi, M. Metz and E. I. Solomon, *J. Phys. Chem. A*, 2002, **106**, 2994–3007.
58. E. I. Solomon, R. K. Szilagyi, S. DeBeer George and L. Basumallick, *Chem. Rev.*, 2004, **104**, 419–458.
59. F. Neese and E. I. Solomon, *Inorg. Chem.*, 1998, **37**, 6568–6582.
60. B. Gu and I. Franco, *J. Phys. Chem. Lett.*, 2018, **9**, 773–778.
61. R. L. Harlow, W. J. Wells, G. W. Watt and S. H. Simonsen, *Inorg. Chem.*, 1974, **13**, 2106–2111.
62. P. Cassidy and M. A. Hitchman, *Inorg. Chem.*, 1977, **16**, 1568–1570.
63. A. A. Gewirth, S. L. Cohen, H. J. Schugar and E. I. Solomon, *Inorg. Chem.*, 1987, **26**, 1133–1146.
64. J. Ferguson, *J. Chem. Phys.*, 1964, **40**, 3406–3410.

65. M. Shiddiq, D. Komijani, Y. Duan, A. Gaita-Ariño, E. Coronado and S. Hill, *Nature*, 2016, **531**, 348–351.
66. G. Wolfowicz, A. M. Tyryshkin, R. E. George, H. Riemann, N. V. Abrosimov, P. Becker, H.-J. Pohl, M. L. W. Thewalt, S. A. Lyon and J. J. L. Morton, *Nat. Nanotechnol.*, 2013, **8**, 561–564.
67. G. Wolfowicz, S. Simmons, A. M. Tyryshkin, R. E. George, H. Riemann, N. V. Abrosimov, P. Becker, H.-J. Pohl, S. A. Lyon, M. L. W. Thewalt and J. J. L. Morton, *Phys. Rev. B*, 2012, **86**, 245301.
68. S. Ghosh, S. Datta, L. Friend, S. Cardona-Serra, A. Gaita-Ariño, E. Coronado and S. Hill, *Dalton Trans.*, 2012, **41**, 13697–13704.
69. A. J. Fielding, S. Fox, G. L. Millhauser, M. Chattopadhyay, P. M. H. Kroneck, G. Fritz, G. R. Eaton and S. S. Eaton, *J. Magn. Reson.*, 2006, **179**, 92–104.
70. J. M. Flowers, J. C. Hempel, W. E. Hatfield and H. H. Dearman, *J. Chem. Phys.*, 1973, **58**, 1479–1486.
71. D. Collison, B. Gahan, C. D. Garner and F. E. Mabbs, *J. Chem. Soc. Dalton Trans.*, 1980, 667–674.
72. C. Finazzo, C. Calle, S. Stoll, S. V. Doorslaer and A. Schweiger, *Phys. Chem. Chem. Phys.*, 2006, **8**, 1942–1953.
73. K. Mrkvová, J. Kameníček, Z. Šindelář, L. Kvítek, J. Mrozinski, M. Nahorska and Z. Žák, *Transit. Met. Chem.*, 2004, **29**, 238–244.
74. M. Warner, S. Din, I. S. Tupitsyn, G. W. Morley, A. M. Stoneham, J. A. Gardener, Z. Wu, A. J. Fisher, S. Heutz, C. W. M. Kay and G. Aeppli, *Nature*, 2013, **503**, 504–508.
75. J. M. Assour, J. Goldmacher and S. E. Harrison, *J. Chem. Phys.*, 1965, **43**, 159–165.
76. A. Noll, S. Rabe and U. Müller, *Z. Für Naturforschung B*, 1999, **54**, 591–596.
77. V. Nagarajan, B. Müller, O. Storcheva, K. Köhler and A. Pöppl, *Res. Chem. Intermed.*, 2007, **33**, 705–724.
78. B. L. Vallee and R. J. Williams, *Proc. Natl. Acad. Sci.*, 1968, **59**, 498–505.
79. B. G. Malmström, *Eur. J. Biochem.*, 1994, **223**, 711–718.
80. R. J. P. Williams, *Eur. J. Biochem.*, 1995, **234**, 363–381.
81. H. B. Gray, B. G. Malmström and R. J. P. Williams, *JBIC J. Biol. Inorg. Chem.*, 2000, **5**, 551–559.
82. S. Ghosh, X. Xie, A. Dey, Y. Sun, C. P. Scholes and E. I. Solomon, *Proc. Natl. Acad. Sci.*, 2009, **106**, 4969–4974.
83. M.-L. Tsai, R. G. Hadt, N. M. Marshall, T. D. Wilson, Y. Lu and E. I. Solomon, *Proc. Natl. Acad. Sci.*, 2013, **110**, 14658–14663.
84. M. W. Mara, R. G. Hadt, M. E. Reinhard, T. Kroll, H. Lim, R. W. Hartsock, R. Alonso-Mori, M. Chollet, J. M. Glownia, S. Nelson, D. Sokaras, K. Kunnus, K. O. Hodgson, B. Hedman, U. Bergmann, K. J. Gaffney and E. I. Solomon, *Science*, 2017, **356**, 1276–1280.
85. L. Kohler, R. G. Hadt, D. Hayes, L. X. Chen and K. L. Mulfort, *Dalton Trans.*, 2017, **46**, 13088–13100.
86. B. Dicke, A. Hoffmann, J. Stanek, M. S. Rampp, B. Grimm-Lebsanft, F. Biebl, D. Rukser, B. Maerz, D. Göries, M. Naumova, M. Biednov, G. Neuber, A. Wetzel, S. M. Hofmann, P. Roedig, A. Meents, J. Bielecki, J. Andreasson, K. R. Beyerlein, H. N. Chapman, C. Bressler, W. Zinth, M. Rübhausen and S. Herres-Pawlis, *Nat. Chem.*, 2018, **10**, 355–362.
87. J. Stanek, A. Hoffmann and S. Herres-Pawlis, *Coord. Chem. Rev.*, 2018, **365**, 103–121.

88. B. E. R. Snyder, P. Vanelderen, M. L. Bols, S. D. Hallaert, L. H. Böttger, L. Ungur, K. Pierloot, R. A. Schoonheydt, B. F. Sels and E. I. Solomon, *Nature*, 2016, **536**, 317–321.
89. P. Comba, S. Fukuzumi, C. Koke, B. Martin, A.-M. Löhr and J. Straub, *Angew. Chem. Int. Ed.*, 2016, **55**, 11129–11133.
90. Y.-I. Sohn, S. Meesala, B. Pingault, H. A. Atikian, J. Holzgrafe, M. Gündoğan, C. Stavrakas, M. J. Stanley, A. Sipahigil, J. Choi, M. Zhang, J. L. Pacheco, J. Abraham, E. Bielejec, M. D. Lukin, M. Atatüre and M. Lončar, *Nat. Commun.*, 2018, **9**, 1–6.